2

CO_2 Laser Photoacoustic Spectroscopy: II. Instrumentation and Applications

Dan C. Dumitras, Ana Maria Bratu and Cristina Popa
Department of Lasers, National Institute for Laser, Plasma, and Radiation Physics, Bucharest Romania

1. Introduction

In this chapter, the main components of an instrument based on laser photoacoustic spectroscopy (LPAS) principles are described in detail. Special emphasis is laid on the home-built, frequency-stabilized, line-tunable CO_2-laser source and the resonant photoacoustic cell. All of the parameters that are characteristic to the photoacoustic cell, including the limiting sensitivity of the system, are measured and compared with the best results reported by other authors. Approaches to improve current sensor performance are also discussed. Other aspects of a functional photoacoustic instrument, such as the gas handling system and data acquisition and processing, are outlined.

Two experimental set-ups were designed and characterized with the photoacoustic (PA) cell in an external configuration: the first one with a low power CO_2 laser where the saturation effects are negligible, and a second one with a high power CO_2 laser where the saturation effects are important. In the first case, the minimum detectable concentration was 0.9 ppbV (parts per billion by volume), while in the second case this parameter was improved to 0.21 ppbV. Comparing with the best results published previously in the literature, our minimum detectable concentration is better by a factor of 4.2 in the first case and by a factor of 18 in the second case.

The next section is dealing with several applications developed in our laboratory. We present a precise measurement of the absorption coefficients of ethylene and ammonia at CO_2 laser wavelengths. For ethylene, the values obtained at 10-μm band excellently agree with other measurements reported in the literature, while important differences were found for the absorption coefficients at 9-μm band. Other applications in plant physiology and medicine (lipid peroxidation and measurement of human biomarkers) are briefly reviewed.

Exhaled breath air analysis represents an attractive and promising novel approach for noninvasive detection of human biomarkers associated with different diseases. Due to extremely low level of the substances of interest in exhaled breath air and the interference of many components at a given laser wavelength, we investigated several measures to increase the accuracy for a single trace gas measurement: a) We studied the efficiency of absorptive trapping and cryogenic trapping to remove carbon dioxide and water vapors from exhaled breath samples. As a result, we found the minimum volume for the KOH trap and the optimum flow rate for transferring gas samples from collecting bags to the photoacoustic (PA) cell. b) We refined breath sample collection procedures from patients under medical

treatment: alveolar collection vs. mixed expiratory collection; collecting bags; preparation of patients (antiseptic mouthwash, avoiding food for at least 12 hours); clean transfer of the gas samples from disposable bags to the PA cell in less than 6 hours. c) We measured the photoacoustic signal at different CO_2 laser wavelengths to distinguish the influence of various absorbent gas components in the total content.

One study involved assessment of breath ethylene and ammonia levels in patients with renal failure receiving hemodialysis (HD) treatment. Our measurements demonstrated that HD determines simultaneously a large increase of ethylene concentration in the exhaled breath (due to the oxidative stress) and a reduction of the ammonia concentration, correlated to the blood urea nitrogen level. Analysis of ethylene and ammonia traces from breath may provide insight into severity of oxidative stress and metabolic disturbances and give information for determining efficacy and endpoint of HD.

2. Experimental arrangement

2.1 General schematic

The block diagram of the laser photoacoustic spectrometer was presented in the previous chapter (Fig. 2, Part I). The cw, tunable CO_2-laser beam is chopped, focused by a ZnSe lens, and introduced in the PA cell. After passing through the PA cell, the power of the laser beam is measured by a laser radiometer Rk-5700 from Laser Probe Inc. with a measuring head RkT-30. Its digital output is introduced in the data acquisition interface module together with the output from the lock-in amplifier. All experimental data are processed and stored by a computer (Dumitras et al., 2007). The frequency stabilized, line tunable CO_2 lasers (low power and high power, respectively) will be described in the next section. Both CO_2 lasers are used in two parallel measuring lines, where two independent experiments can be conducted simultaneously. A view of the two parallel measurement lines with laser photoacoustic sensors is shown in Fig. 1.

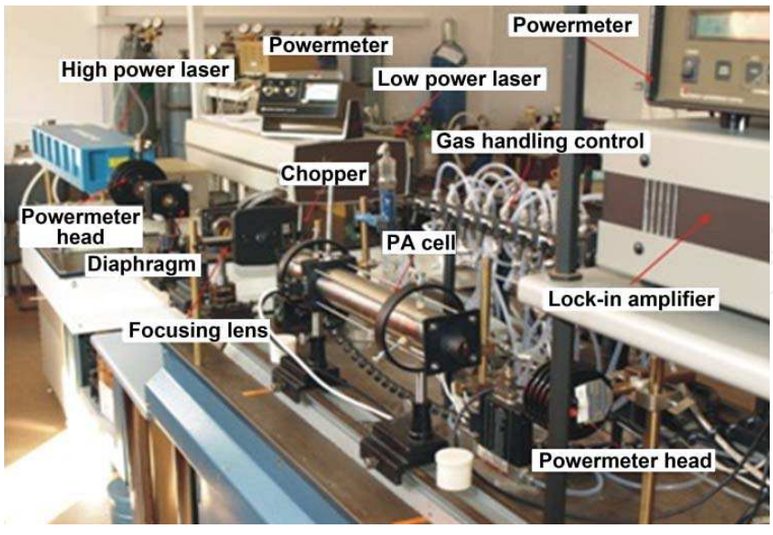

Fig. 1. General view of the PA sensors (two parallel measurement lines).

We decided to use an extracavity arrangement because it has several advantages. In spite of a lower laser power available to excite the absorbing gas in the PA cell, a smaller coherent

photoacoustic background signal makes it possible to increase the overall sensitivity of the instrument. This was proved by comparing our results with those obtained with intracavity arrangements (see Table 3). Also, the dynamic range of the PA method is considerably reduced by intracavity operation. Optical saturation may occur for molecules with high absorption cross section while uncontrollable signal changes may be obtained at higher overall absorption in the PA cell, because the loss of light intensity influences the gain of the laser. This effect may cause erroneous results when the sample concentration changes are large. Therefore, high-sensitivity single- and multipass extracavity PA detectors offer a simpler alternative to intracavity devices.

Various modulation methods are applied in PA spectroscopy. It is necessary to distinguish between the modulation of incident radiation and that of sample absorption (Sigrist et al., 1989). The first schemes include the widely used amplitude modulation of the incident radiation by mechanical choppers, electro-optic and acousto-optic modulators as well as the modulation of the laser emission itself by pulsed excitation, Q-switching, and mode-locking. On the other hand, frequency or wavelength modulation of the incident radiation provides the advantage of eliminating the continuum background PA signal caused by wavelength-independent absorption, e.g., by the cell window. The absorption characteristics of the sample can be modulated based on the Zeeman or Stark effect, i.e., by applying modulated magnetic or electric fields to the sample. Consequently, the absorption wavelength of the sample is varied, which corresponds to a wavelength modulation method. The continuum background is suppressed as a result. For example, a reduction of the background by a factor of 500 was achieved by Stark modulation compared with the one obtained in the same PA cell with conventional amplitude modulation by a chopper (Kavaya et al., 1979). However, it should be noted that the application of the Stark modulation scheme in trace gas detection is restricted to molecules with a permanent electric dipole moment like ammonia (NH_3), nitric oxide (NO), etc. Nevertheless, a considerable increase in sensitivity and, even more important, in selectivity in multicomponent mixtures can be achieved.

The light beam was modulated with a high quality, low vibration noise and variable speed (4-4000 Hz) mechanical chopper model DigiRad C-980 or C-995 (30 slot aperture) operated at the appropriate resonant frequency of the cell (564 Hz). The laser beam diameter is typically 5 mm at the point of insertion of the chopper blade and is nearly equal to the width of the chopper aperture. An approximately square waveform was produced with a modulation depth of 100% and a duty cycle of 50% so that the average power measured by the powermeter at the exit of the PA cell is half the cw value. By enclosing the chopper wheel in a housing with a small hole (10 mm) allowing the laser beam to pass, chopper-induced sound vibrations in air that can be transmitted to the microphone detector as noise interference are reduced. A phase reference signal is provided for use with a lock-in amplifier.

The generated acoustic waves are detected by microphones mounted in the cell wall, whose signal is fed to a lock-in amplifier locked to the modulation frequency. The lock-in amplifier is a highly flexible signal recovery and analysis instrument, as it is able to measure accurately a single-frequency signal obscured by noise sources many thousands of times larger than itself. It rejects random noise, transients, incoherent discrete frequency interference and harmonics of measurement frequency. A lock-in measures an ac signal and produces a dc output proportional to the ac signal. Because the dc output level is usually greater than the ac input, a lock-in is termed an amplifier. The lock-in can also gauge the phase relationship of two signals at the same frequency. A demodulator, or phase-sensitive

detector (PSD), is the basis for a lock-in amplifier. This circuit rectifies the signals coming in at the desired frequency. The PSD output is also a function of the phase angle between the input signal and the amplifier's internal reference signal generated by a phased-locked loop locked to an external reference (chopper). We used a dual-phase, digital lock-in amplifier Stanford Research Systems model SR 830 with the following characteristics: full scale sensitivity, 2 nV - 1 V; input noise, 6 nV (rms)/ $\sqrt{\text{Hz}}$ at 1 kHz; dynamic reserve, greater than 100 dB; frequency range, 1 mHz – 102 kHz; time constants, 10 μs – 30 s (reference > 200 Hz), or up to 30000 s (reference < 200 Hz).

The diverging IR laser beam is converged by a ZnSe focusing lens (f = 400 mm). In this way, a slightly focused laser beam is passed through the photoacoustic cell without wall interactions. The laser beam diameter $D = 2w$ (or its radius, w), which is a very important issue in LPAS, was calculated at different locations on the beam's propagation path (Fig. 2). A too large beam compared to the inner diameter of the resonant tube could increase the coherent photoacoustical background signal to impracticable values. The calculation was made in three steps: a) inside the laser cavity; b) between the laser coupling mirror and the focusing lens, and c) after the focusing lens (including at the center of the PA cell and at the Brewster windows of the cell).

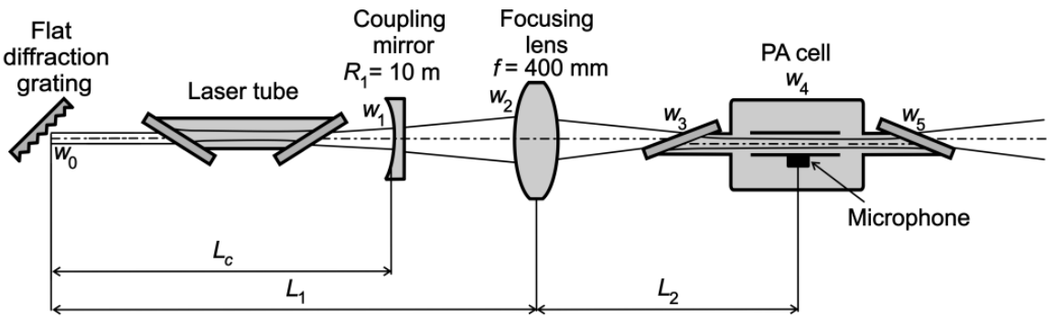

Fig. 2. Geometry of the laser beam from its waist to the exit of the PA cell.

The laser resonator has a stable-type configuration, being made of a diffraction grating equivalent to a totally reflecting flat mirror and a coupling concave spherical mirror with the radius of curvature R_1 = 10 m. We have calculated the parameters of the ideal gaussian beam inside and outside the laser resonator, i.e., for M^2 = 1, and we have obtained the following values: w_0 = 2.91 mm (or a beam waist diameter $2w_0$ = 5.83 mm); w_1 = 3.02 mm ($2w_1$ = 6.04 mm); w_2 = 3.16 ($2w_2$ = 6.32 mm); w_3 = 1.75 mm ($2w_3$ = 3.51 mm); w_4 = 0.51 mm ($2w_4$ = 1.03 mm) and w_5 = 2.26 mm ($2w_5$ = 4.53 mm) (for L_c = 690 mm, L_1 = 1060 mm and L_2 = 450 mm). It follows that as the laser beam travels along the PA cell, its diameter is small enough compared to the diameter of the resonant tube (7 mm) to avoid wall absorptions, which ensures that the chosen geometry minimizes the coherent photoacoustical background signal, as intended.

The pertinent questions we set out to answer in assessing the performance of our PA cell were whether the chosen geometry minimized the coherent background signal, and how sensitive the background and calibration were to slight beam deviations from the intended path. Obviously, if the calibration would vary significantly with small movements of the beam, the accuracy of measurements made with the PA cell would be adversely affected unless the cell alignment was very carefully adjusted and rigidly fixed.

The variation of the background and calibration with transversal or longitudinal translation of the PA cell against the propagation beam direction is very small as long as the laser beam does not strike the walls of the cell. The optimum position of the PA cell against the focusing lens (the center of the resonant tube, i.e. the position of the microphones) is 450 mm (for a focusing length of 400 mm). On extending this optimum distance by 30 mm, the signal is decreased by 0.14%, while when shortening the distance by 60 mm, the signal decreases by 0.61%. The dependence of both signal and background signal on the transversal position of the resonant tube relative to the laser beam is similarly low. We found that the cell calibration and background were virtually invariable for reasonably small longitudinal or transversal movements of the cell.

As the angle of incidence deviates from the Brewster angle θ_B (θ_B = arctan$n$ = 67.38° for ZnSe, where n is the refraction index of the material), the window reflectivity becomes nonzero, and the reflected beam can heat the walls of the cell, making a further contribution to the background signal. Nevertheless, for a ± 10% variation of the angle of incidence relative to the Brewster angle, the reflectance increases from zero to only 2.7% and 1.7%, respectively, meaning that a small deviation from the Brewster angle will not change dramatically the reflectance or the angle of refraction.

Another variable we investigated was the polarization angle of the beam. The cell response in terms of background signal displays a rather broad flat minimum, provided the incidence angle on the window ensures a minimum reflection loss. The data indicate that a deviation of several degrees from vertical polarization can be tolerated. In conclusion, we found that the calibration and background signal were not extremely sensitive to slight misalignments of the beam.

Several authors employed an iris diaphragm in close proximity of the PA cell entrance window to provide spatial filtering in order to reduce the background noise signal caused by off-axis radiation impinging on the internal wall of the chamber. With such a diaphragm, we found that the background signal increased significantly owing to laser beam diffraction at the edges of the aperture. Using high quality optical components (diffraction grating, coupling mirror, lens and windows) together with a well controlled laser beam makes the insertion of an iris diaphragm in the PA instrument unnecessary.

2.2 CO_2 lasers

We have designed, constructed and optimized a rugged sealed-off CO_2 laser (named LIR-25 SF), step-tunable on more than 60 vibrational-rotational lines and frequency stabilized by the use of plasma tube impedance variations detected as voltage fluctuations (the optovoltaic method) (Dumitras et al., 1981; Dumitras et al., 1985; Dutu et al., 1985). The glass tube has an inner diameter of 7 mm and a discharge length of 53 cm. At both ends of the tube we attached ZnSe windows at Brewster angle. The laser is water cooled around the discharge tube. The dc discharge is driven by a high-voltage power supply. The end reflectors of the laser cavity are a piezoelectrically driven, partially (85%) reflecting ZnSe mirror at one end and a line-selecting grating (135 lines/mm, blazed at 10.6 μm) at the other. Piezoelectric ceramics such as lead zirconate titanate (PZT) can be used.

A free-running or unstabilized laser is subject to many perturbations of its frequency. First of all, changes in cavity length affect the frequency of an oscillating mode ($\Delta\nu/\nu = \Delta L/L$), so keeping a constant length is the prime objective in frequency stabilization schemes. Possible perturbations of the cavity length can be divided into two groups: external effects (thermal

variations of the spacer material, changes in atmospheric conditions, mechanical vibrations, variations in the position of optical components and in magnetic fields) and internal effects, which are generally related to the discharge noise.

Active power stabilization based on a piezo-driven out-coupling mirror is used in our laser. The principle of the stabilization schemes is based on a comparison between the frequency of a single frequency laser (single-mode, single-line) and some stable point of reference. If the laser frequency is different from that of the benchmark, an error-sensing discriminant is used to derive a signal proportional to the deviation. This error signal is used to control the laser oscillating frequency and retune it to the reference one. Such a servo-loop (closed loop feedback) locks the laser frequency to that of the reference. For moderate stability, the CO_2 laser line profile can be used as the discriminating curve (Dumitras et al., 1981). This method is more appropriate for the CO_2 laser than for other lasers because the CO_2 vibrational-rotational line profile is narrow and has much steeper slopes than, for example, that of the neon line in a He-Ne laser. The error signal is produced by allowing the laser resonance cavity to "ride" around the steep part of the line profile slope, and its amplitude is dependent on the change in cavity mirror separation. This scheme requires internal frequency modulation (jittering) of the laser in order to sense the sign of the derived error signal. Stabilization is then obtained by re-establishing the required separation with a servo-system.

The CO_2 laser is frequency stabilized to the center of the curve representing its output power *versus* frequency (the molecular resonance) upon the variation of plasma tube impedance, when the optical power extracted from the medium is modulated (Dutu et al., 1985). In this closed-loop active stabilization, the cavity length is controlled by a piezoelectrically driven mirror along the cavity axis, which responds to the sum of a dc control voltage, plus a small jitter signal at some convenient frequency (~500 Hz). As can be seen in Fig. 3, where a curve of laser line gain *versus* frequency is drawn, the small cavity jitter induces a sinusoidal variation in laser output as the cavity mode scans across the transition gain profile, which is compared in phase to the jitter voltage.

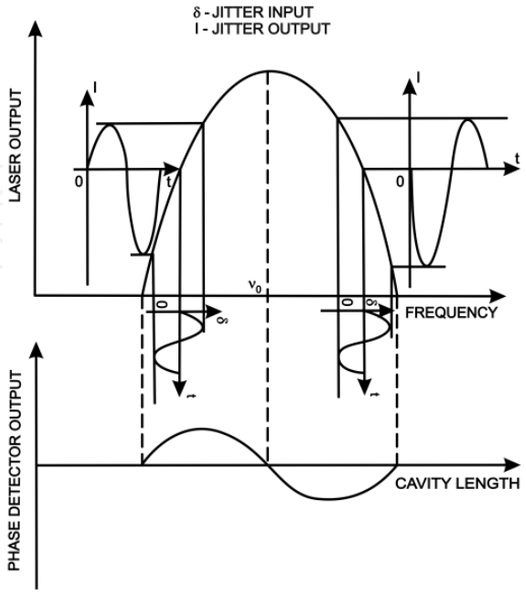

Fig. 3. Generation of the error-frequency signal.

The error signal generated by the phase detector can serve to drive the cavity resonance to the center of the laser gain curve. In this way, the electronic feedback loop seeks the center of the lasing gain profile, the lock-in point being the zero crossing of the phase detector response. If the mean mode frequency is lower than the line center frequency, the phase of the observed laser intensity variation is opposite to the one we have where the mode frequency is higher than the line center frequency. The amplitude of the jitter output increases with the frequency offset from the line center.

In lieu of using an IR detector to sense the laser intensity variation, the cavity length is adjusted using the optovoltaic effect. As the internal laser radiation field intensity is altered by changing the resonant cavity alignment, the discharge impedance, which is proportional to the slope of the curve of laser output power *versus* frequency, is also modulated. The impedance variation is determined by exciting the plasma tube with a high-speed current-regulated power supply and measuring the resulting variation in the voltage drop across the plasma tube (the optovoltaic effect). An intensity variation of 1% is sufficient to change the discharge impedance significantly (~ 0.1%). By using a current regulated power supply, the voltage impedance fluctuation is detected as an ac component of the voltage drop across the plasma tube.

Before any attempt is made to stabilize the frequency of a laser, a single frequency output must be ensured. For this purpose, a laser operating in the lowest transversal mode (TEM_{00}) must be designed (Dumitras et al., 1976). The single line operation of the CO_2 laser is achieved with a dispersive element (diffraction grating). The cavity length of L_c = 690 mm corresponds to a separation between two longitudinal modes of $\Delta\nu = c/2L_c$ = 217 MHz. Calculating the collisional broadening in a mixture of CO_2, N_2, He, Xe, and H_2 at a total pressure of 34 mbar gives a collisional full linewidth at half maximum (FWHM) $\Delta\nu_c$ = 119 MHz. We therefore conclude that a single frequency operation is obtained when a longitudinal mode is tuned on the top of the gain curve ($\Delta\nu > \Delta\nu_c/2$).

To increase the number of oscillating lines, especially those with a smaller gain, and obtain reliable long term operation at a single specific wavelength, some form of wavelength selection introduced in the optical cavity is generally required. As optical dispersion is incorporated by using a diffraction grating or Brewster-angle prisms within the laser cavity, the laser can be made to oscillate on only one vibrational-rotational line, otherwise the particular transition on which the CO_2 laser operates depends on the length of the resonator. That is why the total reflecting mirror must be replaced by a diffraction grating, which is tilted about its groove axis to the blaze angle and acts as a frequency selective reflector. Light diffracted into the first order maximum is returned along the optical axis and taken as laser output, while light in other orders as well as any other wavelength is returned off-axis and gets lost. Another advantage of a laser resonator with a grating is that the laser can be tuned over the entire oscillating linewidth from the line center.

We used a flat diffraction grating with 135 grooves/mm, blazed at 10.6 μm and having a peak efficiency of 96%, mounted in a Littrow configuration. With such a grating, the vibrational-rotational lines emitted by the CO_2 laser in the range P(50) – 10.9329 μm and R(44) – 9.1549 μm can be selected by controlling the grating angle in the range 47°33′32′′ to 38°10′02′′, which can be set to the desired laser transition with a micrometric screw. This grating presents a good dispersion, as the P(18) and P(20) lines (10.4 μm band) are separated by a 6′38′′ angular difference (as compared with 2′49′′ for a diffraction grating with 75 grooves/mm).

To meet the frequency stability requirements, the laser cavity must be so constructed as to reduce the effects of ambient vibration and thermal variations on the output frequency of the laser. This places less stringent demands on the performance of the servo-system controlling the laser frequency. To minimize the thermal length changes ($\Delta L/L = \alpha\Delta T$) in the mirror support structure, a material with a low expansion coefficient has to be used for the spacers between the endplates of the cavity which carry the mirrors. Such a material is Invar, which has an expansion coefficient $\alpha = 1.26\text{x}10^{-6}/^{o}\text{C}$. To obtain a passive instability of $3\text{x}10^{-8}$ for the laser frequency, the temperature variation must not exceed 0.024^{o}C. Such constant temperature is hard to maintain, especially in longer lasers, where high power inputs and high heat dissipation cause large temperature instabilities.

Stiffness is a most desirable attribute for minimizing fractional changes in the cavity length. Special measures were taken against mechanical vibrations (by eliminating high frequency vibrations), variations in the position of optical components (by supporting rigidly any intracavity element) as well as to prevent magnetic fields and acoustically borne vibrations, which can be reduced by shielding the laser with some form of enclosure. The design of the remaining structure was chosen so as to avoid the lowering of the basic first resonance. The joints between the elements of the structure, especially the joints perpendicular to the laser axis, were so designed that they did not have any low frequency resonances. To have a spring constant of the joint high enough and to avoid joints using only the spring force of a few screws to connect significant masses, we used large contact areas under compressional stress. We chose a cylindrical shape for the mechanical structure, including the housing, because of its high resistance to bending deformation. A section through the laser cavity assembly is given in Fig. 4 and a photo of the mechanical structure, laser tube, and control panel is presented in Fig. 5.

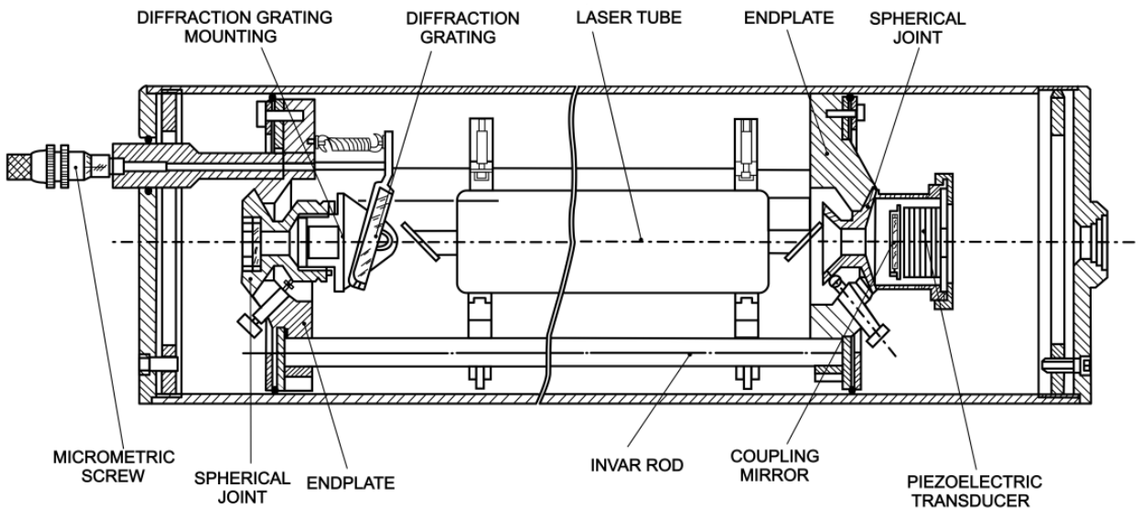

Fig. 4. Longitudinal section through the laser cavity assembly.

To keep the weight unchanged and still maintain the required thermal characteristics, the endplates of the cavity which carry the mirror and the diffraction grating were primarily constructed of aluminum. The three invar rods are potted into the aluminum frame so as to ensure intimate contact between the invar rods and the rigid aluminum structure. To remove the problems associated with weak spring-type controls, the mirror holders were designed

ruggedly. The mirrors can be adjusted in angle by sliding two stainless steel spherical joints with respect to one another. As the mirrors are adjusted into their final position, the adjustment screws clamp the mirror holder tightly so that no inadvertent movement is possible.

Fig. 5. Homebuilt frequency stabilized CO_2 laser model LIR-25 SF.

The diffraction grating is mounted in a similar holder and is rotated by a micrometric screw (0 – 25 mm), as shown in Fig. 6. The laser tube was rigidly mounted in the cavity with two concentric rings, the inner one being adjusted by three screws. This system allows the laser tube axis to fall into line with the mirror centers and provides good transverse stability.

Fig. 6. Diffraction grating-drive mechanism.

To achieve active stabilization, an automatic frequency control circuit (lock-in stabilizer) is used to maintain an axial mode on the top of the gain curve. The block diagram of the frequency stabilization system based on plasma tube impedance variations is shown in Fig. 7. A sinusoidal signal with a rough frequency of 500 Hz derived from the pilot oscillator is applied to the piezoelectric transducer, resulting in a simultaneous frequency and amplitude modulation of the laser output, dependent on the amplitude of the sinusoidal signal.

The ac voltage drop across the tube is passed through a tuned amplifier and then synchronously detected. The demodulation of the ac signal is performed in the phase-sensitive detector, with phase (continuously adjustable) determined by the phase shift

circuit. The demodulator output is processed by the operational integrator and a high voltage dc amplifier. The dc bias together with this error correction signal is applied to the piezoelectric transducer, thus closing the feedback loop. The error signal generated by the phase detector serves to drive the cavity resonance to the center of the laser gain curve and compensates for the effects of slow drift.

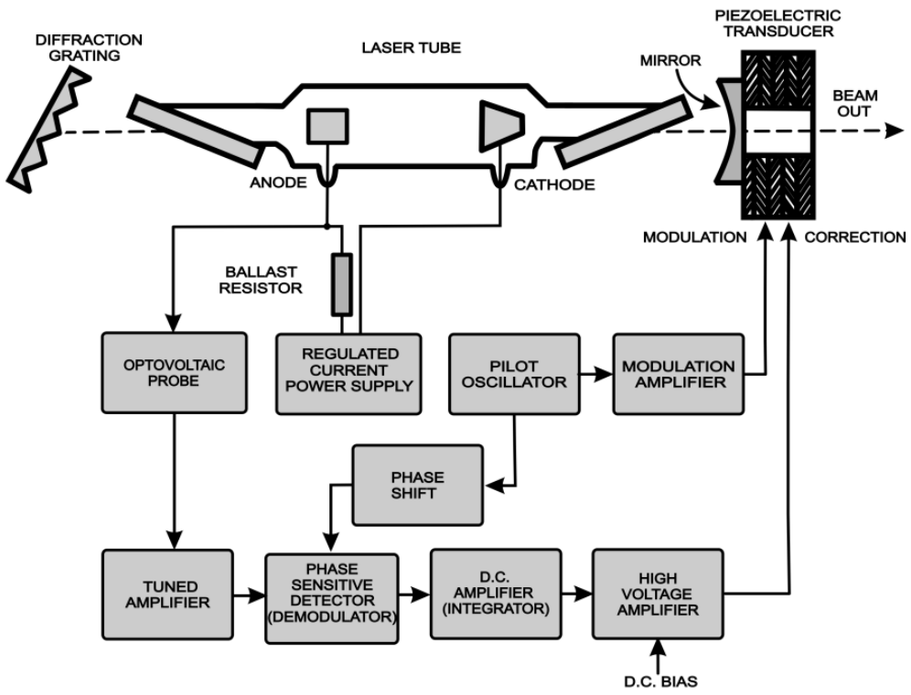

Fig. 7. Block-diagram of the automatic frequency control electronics.

There are fifteen functional modules grouped into three main blocks in accordance with the specific function they play in the operation of the frequency stabilized CO_2 laser:

1. a high speed current regulated power supply, which excites the cw CO_2 laser tube;
2. a servo control system, which controls the length of the resonant cavity;
3. a logic electronic system which allows an efficient operative control and monitoring of the frequency stabilized CO_2 operation.

The high-speed current regulated power supply includes three modules namely: the power supply converter – PSC, the power supply feedback – PSF, and the power supply rectifier PSR. The high frequency of the converter makes it possible to minimize the electronic components that are used in making the high voltage transformer and the low pass filter of the high voltage rectifier.

The modulation signal that is needed to scan the laser line profile is generated by a pilot oscillator and applied to the piezoelectric transducer through a modulation amplifier. Both circuits are placed on the same functional module OMA (Oscillator & Modulation Amplifier). For cw CO_2 lasers excited by current regulated power supplies, the modulation signal which appears in the emitted radiation can be measured according to the optovoltaic effect using a simple band pass filter like that noted with OVP (Optovoltaic Probe). The detected optovoltaic signal is amplified through a two-stage tuned ac amplifier – ACA. The amplified optovoltaic

signal is introduced in the phase sensitive detector (PSD module) together with a phase adjustable component of the reference signal from the modulation oscillator.

The error signal is obtained in the output of the electronic dc amplifier module DCA, by processing the output signal of the phase sensitive detector. The DCA module has two modes of operation, namely: (a) gain of ten amplifier with integrating time constant of 1 second; (b) high gain integrator with output slewing rate of about 6 V/s per volt of input. The first mode allows the observation of smoothed output of the demodulator (stabilization discriminator), while the second one is used in closed loop stabilization to observe the error signal. A high voltage amplifier (HVA) that works on the principle of a switching high voltage power supply drives the piezoelectric transducer under the control of the error signal.

The logic electronic system includes four specialized modules, namely: a low voltage stabilized power supply (SPS), a logic drive circuit (LDC), a power meter circuit for laser radiation (PMC), and a beam controller (BCS). Every parameter and state that are monitored or selected in the operation of the frequency stabilized CO_2 laser LIR-25 SF are displayed on the rear panel of the laser (Fig. 5) by means of nine light emitting diodes (LED) driven by the panel display circuit (PDC). The output beam of the laser can be sent to either the powermeter head or the exit by a two-position reflecting mirror, controlled by a beam shutter circuit and a beam selector switch placed on the rear panel.

The long-term frequency instability was $\Delta\nu/\nu = 3\text{x}10^{-8}$ or $\Delta\nu = 1$ MHz ($3\text{x}10^{-5}$ cm^{-1}).

A supplementary power stabilization is possible by using an additional feedback loop (Dumitras et al., 2006). The principle used for power stabilization took into account the dependence of the output power on discharge current. The new feedback loop (Fig. 8) modifies the discharge current so to maintain the output power at a constant value imposed by the reference.

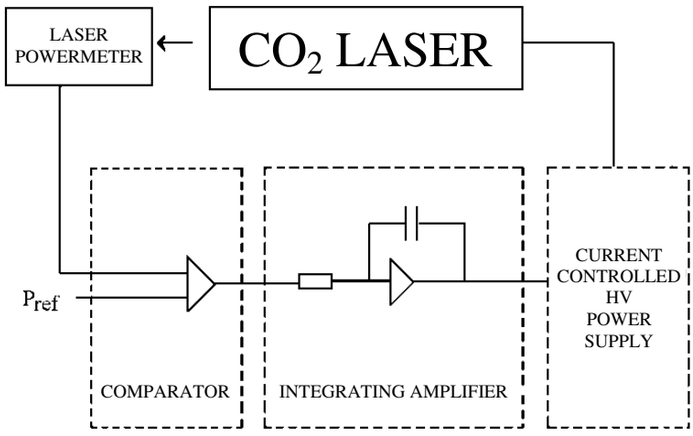

Fig. 8. Supplementary feedback loop used for laser power stabilization.

The performance of the two feedback loops used for frequency and power stabilization of the CO_2 laser were evaluated by using computer data acquisition. It was monitored simultaneously the output power, the discharge current and the temperature inside laser cavity, while the power instability was calculated for a period of 2 minutes. The importance of the two feedback loops to reduce the output power instability can be remarked from these measurements. Thus, when both the frequency stabilization loop and the power

stabilization loop are opened and forced hot air perturbation is introduced, the power instability is 10.2%, a value too large for many applications; when the frequency stabilization loop is closed and the power stabilization loop is opened (no perturbation), the power instability is reduced to 1.06%; when the frequency stabilization loop is closed and the power stabilization loop is opened and forced hot air perturbation is introduced into laser cavity, the power instability increases only a little, to 1.57%; and when both the frequency stabilization loop and the power stabilization loop are closed and forced hot air perturbation is introduced, the power instability is reduced drastically, to 0.28%. If there is no perturbation and the two feedback loops are closed, the power instability is only 0.23%. In conclusion, the power instability was reduced by four times with this supplementary feedback loop, from 1% to as low as 0.23% for a period of 2 minutes.

The tunability of our CO_2 laser is presented in Fig. 9. We observed the oscillation of 62 different vibrational-rotational lines in both the 10.4 μm and 9.4 μm bands. In this way, the laser was line tunable between 9.2 μm and 10.8 μm with powers varying between 1 and 6.5 W depending on the emitted laser transition. More than 20 lines had output powers in excess of 5 W.

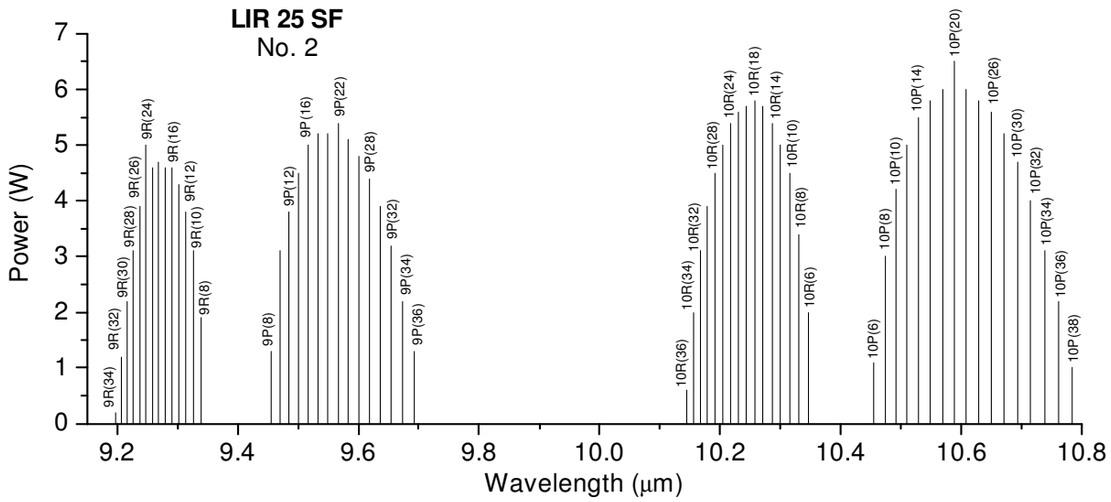

Fig. 9. Tunability of the low power CO_2 laser with diffraction grating: P(max) = 6.5 W; Tunability: 9R(8) – 9R(34); 9P(8) – 9P(36); 10R(6) – 10R(36); 10P(6) – 10P(40); No. of lines: 62.

Fig. 10. Coherent GEM SELECT 50™ CO_2 laser in the experimental setup.

To investigate the possibility of using a high power laser in an extracavity configuration, we introduced in the experimental set-up a commercial CO_2 laser (Coherent GEM SELECT 50™ laser) (Fig. 10) with output power till 50 W and tunable on 73 different lines (Fig. 11). When this laser is tuned on 10P(14) line, the maximum power delivered after chopper and focusing lens is 14.5 W.

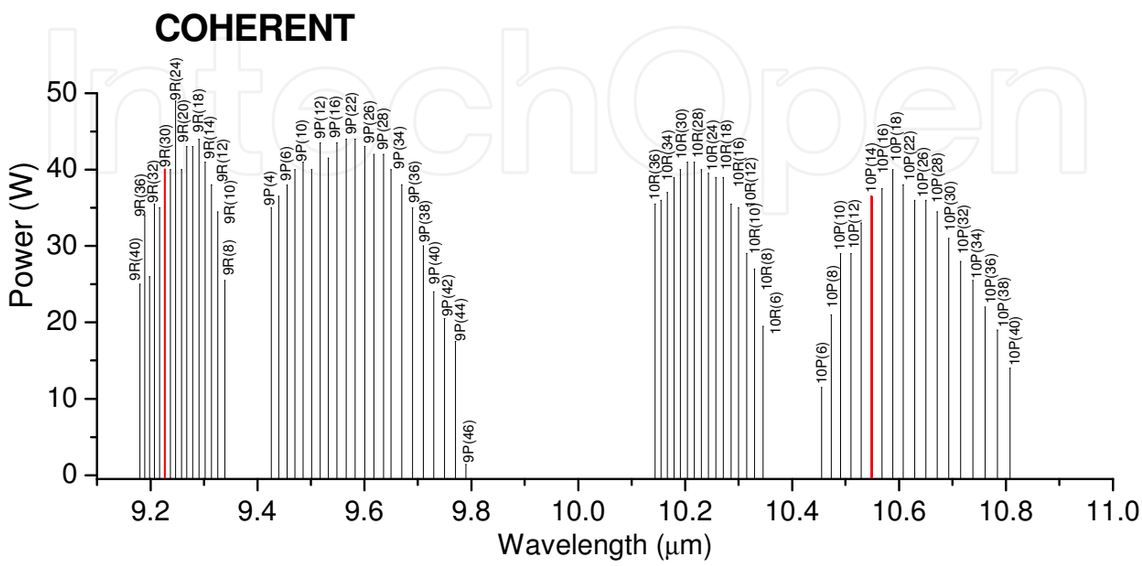

Fig. 11. Tunability of the high power CO_2 laser with diffraction grating: P(max) = 50 W; Tunability: 9R(8) – 9R(40); 9P(4) – 9P(46); 10R(6) – 10R(36); 10P(6) – 10P(40); No. of lines: 73 (10P(14): λ = 10.53 μm; 9R(30): λ = 9.22 μm).

2.3 Photoacoustic cell

In the literature the PA cells are often characterized as "nonresonant" or "resonant". This terminology is misleading, because any PA cell can be operated at an acoustic resonance or far from its resonance. Thus, it is preferable to label the system in terms of its nonresonant or resonant mode of operation.

To design an optimum acoustically resonant PA cell to be used in CO_2 laser photoacoustic spectroscopy, the following requirements have to be met:

i. the fraction of laser energy absorbed by the gas must be maximized by increasing either the incident laser power (but maintaining a large SNR) or the optical density of the gas (Eq. 2, Part I);
ii. cell responsivity needs to be as high as possible, because the voltage response is proportional to it (Eq. 29, Part I);
iii. the microphone responsivity has to be as high as possible, and the use of many microphones is advisable (Eqs. 30 and 31, Part I);
iv. the design must make it possible to operate the cell at an acoustic resonance, and the resonance frequency must lie between 400 and 1000 Hz, where the microphone noise is minimal;
v. the quality factor Q of the acoustic resonance must not exceed 50 in order to decrease the influence of small deviations from the resonance frequency;

vi. the electrical noise and the coherent acoustic background noise must be as low as possible; this can be done by using low noise microphones, good acoustic and vibration isolation, low noise electronics, and good electronic isolation (no ground loops, proper shielding);
vii. the coherent photoacoustic background signal due to the heating of the walls and windows must be minimized by using optical components of very high quality and introducing acoustic baffles;
viii. the cell must enable continuous gas flow operation, and consequently not only the cell windows, but also the gas inlets and outlets have to be positioned at pressure nodes of the resonance;
ix. the cell must have low gas consumption and fast response, and the cell volume has to be sufficiently small to prevent prohibitive dilution when the produced trace gas is flowed through the cell volume by a continuous gas stream;
x. the adsorption and desorption rates on the surfaces in direct contact with the sample gas that can influence particularly measurements on sealed-off samples must be minimized by using special cell materials and reducing the surface-to-volume ratio;
xi. the effect of the loss mechanisms which we can control must be minimized by an appropriate system design.

Various ways to design (cylindrical geometry, H geometry, T geometry, or using a Helmholtz resonator) and operate (longitudinal, azimuthal, radial, or Helmholtz resonances) resonant PA cells have been studied (Zharov & Letokhov, 1986). Furthermore, PA cells for multipass (Koch & Lahmann, 1978; Nägele & Sigrist, 2000) or intracavity operation (Fung & Lin, 1986; Harren et al., 1990a) were designed. The effect of window heating in the amplitude modulation schemes has been minimized by introducing acoustic baffles (Dewey, 1977), developing windowless cells (Gerlach & Amer, 1980; Miklos & Lörincz, 1989; Angeli et al., 1992), or using tunable air columns (Bijnen et al., 1996). In many cases the window-heating signal can be markedly reduced by positioning the entrance and exit of the light beam at nodes of the mode being excited.

A cylindrical cell operated at a radial resonance and having Brewster windows mounted at the pressure nodes of the first radial mode, as presented by Gerlach and Amer (Gerlach & Amer, 1980), does not fulfill all these requirements. Therefore, an open resonant cell excited in its first longitudinal acoustic mode was developed to fulfill most of these requirements.

The H-type longitudinally resonant cell was chosen to form the core of our measuring instrument. Dividing the PA cell into a central chamber and two buffer chambers adjacent to the Brewster windows, a design which lowered significantly the coherent photoacoustic background noise, was first proposed by Tonelli et al. (Tonelli et al., 1983). The characteristics of this type of PA cell have been discussed by Nodov (Nodov, 1978), Kritchman et al. (Kritchman et al., 1978), and Harren et al. (Harren et al., 1990a). Its main advantages are: (a) stable operation at a relatively low frequency; a quality factor of about 20, i.e., much lower than that of a radial resonator, which makes it less sensitive to environmental changes; the efficient conversion of radial to longitudinal modes and the relatively long wavelength guarantee a sufficiently high photoacoustic amplitude; (b) a longitudinal resonator is not noticeably influenced by the gas flow at the desired flow rate of several L/h; noise by gas flow phenomena is negligible for properly positioned inlet and outlet ports; (c) window noise is minimal if the windows are located at a quarter wavelength from the ends of the resonator tube; (d) the construction is rugged and simple and can be achieved with low adhesion materials.

Following these guidelines, a PA cell was designed, constructed, and tested. An H-type cylindrical cell designed for resonant photoacoustic spectroscopy in gases is shown in Fig. 12. The longitudinal resonant cell is a cylinder with microphones located at the loop position of the first longitudinal mode (the maximum pressure amplitude). Some general considerations imply that the coherent photoacoustic background signal caused by window heating is decreased if the beam enters the cell at the pressure nodes of the resonance. The advantage of mounting the windows at the pressure nodes is well demonstrated, and the window heating signal is decreased by the Q factor. The laser beam enters and exits the cell at the Brewster angle. It is more advantageous to have the beam pass through the windows at the Brewster angle (θ_B), as θ_B is nearly constant over a wide range of wavelengths, and variations of θ_B with wavelength can be tolerated since reflectivity increases very slowly for small deviations from θ_B.

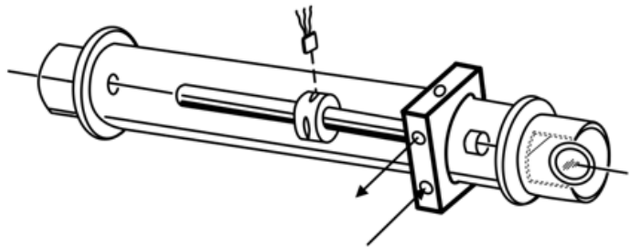

Fig. 12. Schematic of the PA cell designed for the first longitudinal resonance mode.

The influence of scattered light onto the PA background signal can be minimized by using a highly reflecting polished material, with a good thermally conducting substrate. Bijnen et al. (Bijnen et al., 1996) investigated different materials for the resonant tube and found that the background signal decreased for polished stainless steel, polished brass, and polished, gold-coated copper in a ratio of 6:2:1, respectively. In the case of the CO_2 laser, the best performance was obtained by employing a copper tube with a polished gold coating as resonator material. Because of the excellent heat-conducting properties, the absorbed heat can be quickly dispersed in the copper tube. The gold coating was used not only to optimize laser radiation reflection, but also to obtain a noncorrosive surface to withstand aggressive gases.

Many polar compounds (e.g. ammonia) are highly adsorptive and produce an error in real time concentration measurements by adhering to the detector surfaces. These molecules interact strongly with most metals and many insulating materials. Ammonia is a good model compound for these molecules as it shows the characteristic adsorptive behavior that is not a health hazard at low concentrations. The rate of ammonia adsorption on the gas handling surfaces depends on the surface material and temperature, and on the mixture concentration, flow rate, and pressure. Comparing the ammonia results with those for ethylene, which interacts weakly with most surfaces, provides a measure of the cell-sample interaction. Beck (Beck, 1985) evaluated the suitability of several surface materials for minimizing sample adsorption loss. Four materials–304 stainless steel, gold, paraffin wax, and Teflon–were tested using ammonia as a sample. The results show that both metals interact strongly with the sample. Teflon coating (thickness <25 μm) was found to provide accurate real time response for ammonia sample flows. Also, no signal decay is observed following flow termination. Additionally, the coatings must not degrade the acoustic response of the cell. The Teflon coating actually increases the cell Q by a small amount (1 percent). This is attributed to the smooth slick surface obtained by Teflon coating which

would decrease any surface frictional or scattering loss of acoustic energy. Rooth et al. (Rooth et al., 1990) tested the following wall materials – stainless steel 304, gold (on Ni-coated stainless steel), Teflon PTFE, and Teflon PFA – in contact with the gas. Stainless steel proved to be an almost unsaturable reservoir for ammonia at pptV levels. The number of stored molecules exceeded by a factor of 10 or more the number of potential locations on the total geometric surface. Despite its inferior properties in terms of adsorption, Olafsson et al. (Olafsson et al., 1989) used a stainless steel cell for detecting NH_3 and found that an operating temperature of 100°C combined with water vapors led to a very significant reduction of NH_3 adsorption. Apparently, the water molecules stick to the walls even more efficiently than NH_3, and the cell walls are effectively coated with water. Later on, the sample cell was constructed with Teflon as wall material (Olafsson et al., 1992).

Since an open pipe efficiently picks up and amplifies noise from the environment, it should be surrounded by an enclosure. In order to ensure high acoustic reflections at the pipe ends, a sudden change of the cross section is necessary. Therefore, the resonator pipe should open up into a larger volume or to buffers with a much larger cross section. The buffers can be optimized to minimize flow noise and/or window signals. The length of the two buffers accounting for half the resonator length is chosen such as to minimize the acoustic background signal originating from absorption by the ZnSe windows. Open pipes were introduced for PA detection as early as 1977 (Zharov & Letokhov, 1986), and the most sensitive PA detectors currently used are based on open resonant pipes. In resonant cells, window signals can be diminished by using $\lambda/4$ buffers next to the windows. These buffers, placed perpendicular to the resonator axis near the windows, are tuned to the resonator frequency and act as interference filters for the window signals (the coupling of the window signals into the resonator is reduced by large buffer volumes that act as interference dampers).

It was found both theoretically and experimentally that the signal amplitude decreases drastically when buffer length $L_{buf} < \lambda/8$ (Bijnen et al., 1996); the resonance frequency and the quality factor, for both the window and gas signals, are not much affected by changing the buffer length. The length of the buffer is optimal for window signal suppression when $L = 2L_{buf}$ ($L >> r$) (L and r stand for resonator length and radius). The dependence of the gas absorption p_g and window absorption pressure p_w on the ratio of the buffer and resonator radii is:

$$p_g \propto \frac{\sqrt{L}}{r}\left(1-\frac{r^2}{r_{buf}^2}\right), \tag{1}$$

$$p_w \propto \frac{r}{r_{buf}\sqrt{L}}. \tag{2}$$

The ratio between the gas absorption signal and window signal then becomes:

$$\frac{p_g}{p_w} \propto \left(\frac{r_{buf}}{r}\right)^2 L. \tag{3}$$

The optimal buffer length, resulting in an optimal suppression of the photoacoustic background signal, is $\lambda/4$. Choosing a buffer length of $\lambda/8$ has the advantage of a shorter cell, and a good, though not optimal, suppression of the window signal is still possible in this case. If the volume and overall size of the buffers pose no problem, their radii have to be

large for optimal operation. A practical radius can be deduced to be $r_{buf} \approx 3r$. The gas absorption amplitude is barely influenced above this value. A small radius for the resonator of the resonant cell is advantageous as it enhances gas absorption. The limit for the resonator radius is mainly determined by the wings of the gaussian laser beam profile hitting the wall; r should roughly be at least three times the radius of the laser beam to reduce wall absorption to an acceptable level.

Our PA cell design, based on the above considerations, is shown in Fig. 13 in cross sectional longitudinal view. The PA cell is made of stainless steel and Teflon to reduce the outgassing problems and consists of an acoustic resonator (pipe), windows, gas inlets and outlets, and microphones. It also contains an acoustic filter to suppress the flow and window noise. ZnSe windows at the Brewster angle are glued with epoxy (Torr-Seal) to their respective mounts. The resonant conditions are obtained as longitudinal standing waves in an open tube (resonator) are placed coaxially inside a larger chamber. We use an open end tube type of resonator, excited in its first longitudinal mode. To achieve a larger signal (eqs. 26 and 27, Part I), we chose a long absorption path length (L = 300 mm) and an inner diameter of the pipe of $2r$ = 7 mm ($r \cong 1.5w_5$, see Fig. 2). The fundamental longitudinal wave, therefore, has a nominal wavelength $\lambda_s = 2L$ = 600 mm (and a resonance frequency f_0 = 564 Hz). The effective wavelength is ~1% longer than the nominal value, in accordance with predictions of Eq. (5, Part I). The two buffer volumes placed near the Brewster windows have a length L_{buf} = 75 mm ($\lambda/8$) and a diameter $2r_{buf}$ = 57 mm ($r_{buf} \cong 8r$). The inner wall of the stainless steel resonator tube is polished. It is centered inside the outer stainless steel tube with Teflon spacers. A massive spacer is positioned at one end to prevent bypassing of gas in the flow system; the other is partially open to avoid the formation of closed volumes. Gas is admitted and exhausted through two ports located near the ends of the resonator tube. The perturbation of the acoustic resonator amplitude by the gas flow noise is thus minimized.

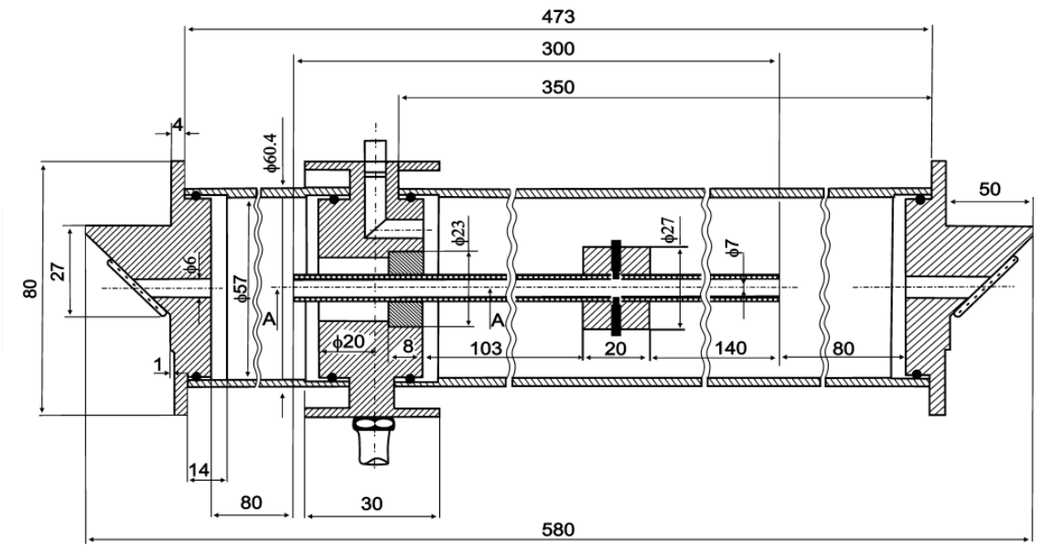

Fig. 13. A resonant photoacoustic cell with buffer volumes.

The total cell volume is approximately 1.0 dm^3 (total length 450 mm, and inner diameter 57 mm, minus inner mechanical parts). For flowing conditions, however, it is advantageous to reduce the active volume of the cell. Especially if the flow rate is smaller than 1 L/h (16.6

sccm - standard cubic centimeters per minute), the replenish time for the 1.0 dm^3 cell becomes impractical. The buffer volume at the entrance port of the cell affects the renewal time τ considerably. The buffer volume is approximately 200 cm^3, yielding a time constant of 12 min ($\tau = V/R_{flow}$ = (200 cm^3)/(16.6 cm^3/min) = 12 min). By reducing the buffer volume to 24 cm^3, with $r_{buf} \cong 3r$ (diameter 20 mm, length 75 mm), a τ of 1.5 min is obtained. However, an increased acoustical noise level was observed, due to the gas flow.

In photoacoustic measurements in the gas phase, microphones are usually employed as sensing elements of the acoustic waves generated by the heat deposition of the absorbing molecules. Although high-quality condenser microphones offer the best noise performance, they are rarely used in photoacoustic gas detection because of their large size, lower robustness, and relatively high price. The most common microphones employed are miniature electret devices originally developed as hearing aids. The choice of a miniature microphone is particularly advantageous since it can be readily incorporated in the resonant cavity without significantly degrading the Q of the resonance. The frequency response of electret microphones extends beyond 10 kHz, and the response to incident pressure waves is linear over many orders of magnitude.

In our PA cells there are four Knowles electret EK-3033 or EK-23024 miniature microphones in series (sensitivity 20 mV/Pa each at 564 Hz) mounted flush with the wall. They are situated at the loops of the standing wave pattern, at an angle of 90° to one another. The microphones are coupled to the resonator by holes (1 mm diameter) positioned on the central perimeter of the resonator. The battery-powered microphones are mounted in a Teflon ring pulled over the resonator tube (Fig. 14). It is of significant importance to prevent gas leakage from inside the resonator tube along the Teflon microphone holder, since minute spacing between the holder and resonator tube produces a dramatic decrease of the microphone signal and the Q value. The electrical output from these microphones is summed and the signal is selectively amplified by a two-phase lock-in amplifier tuned to the chopper frequency.

Fig. 14. Teflon rings used to mount the microphones flush with the tube wall.

The resonance curve of our PA cell (cell response in rms volts) was recorded as a function of laser beam chopping frequency and the results are plotted in Fig. 15. An accurate method is to construct the resonance curve point by point. In this case, the acoustic signal is measured at different fixed frequencies thus avoiding potential problems arising from the slow formation of a steady state standing wave in the resonator and the finite time resolution of the lock-in amplifier. It is evident from these data that the cell resonance curve is fairly broad, implying that the absorption measurements would not be considerably affected if the

frequency of the laser modulation or the cell resonance itself were to shift by a few hertz. PA cells exhibiting narrow resonances (as in the case of excitation of the radial modes) require tight control of both temperature and laser modulation frequency to avoid responsivity losses during the experiment.

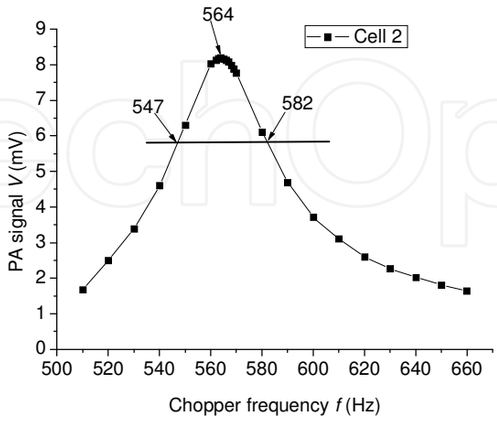

Fig. 15. Resonance curve for the first longitudinal mode of the PA cell.

The acoustic resonator is characterized by the quality factor Q, which is defined as the ratio of the resonance frequency to the frequency bandwidth between half power points. The amplitude of the microphone signal is $1/\sqrt{2}$ of the maximum amplitude at these points, because the energy of the standing wave is proportional to the square of the induced pressure. The quality factor was measured by filling the PA cell with 1 ppmV of ethylene buffered in nitrogen at a total pressure of 1 atm and by tuning the modulation frequency in 10 Hz increments (2 Hz increments near the top of the curve) across the resonance profile to estimate the half width, as described above. For this PA cell, the profile width at half intensity was 35 Hz, yielding a quality factor Q = 16.1 (Eq. 15, Part I) at a resonance frequency f_0 = 564 Hz. The experimentally determined resonance is not completely symmetric, as the curve rises steeply on one side and becomes less steep on the other side of the maximum. This asymmetry is caused by a coherent superposition of the standing acoustic waves in the detection region of the microphones (Karbach & Hess, 1985).

The calibration of the PA system is usually performed with a reference gas. We calibrated our PA cell with the widely used reference gas ethylene, whose absorption coefficients are accurately known at CO_2-laser wavelengths. Ethylene is well suited for this purpose, since it interacts only weakly with common cell surface materials. Ethylene is chemically inert, has the same molecular weight as nitrogen and possesses no permanent dipole moment which means negligible adsorption on the cell walls. Furthermore, its spectrum within the CO_2-laser wavelength range is highly structured. In particular it exhibits a characteristic absorption peak at the 10P(14) laser transition at 949.49 cm^{-1} which is caused by the proximity of the Q branch of the ν_7 vibration of C_2H_4 centered at 948.7715 cm^{-1}. We used a commercially prepared, certified mixture containing 0.96 ppmV C_2H_4 in pure nitrogen throughout our investigations. For calibration we examined this reference mixture at a total pressure p of approximately 1013 mbar and a temperature $T \cong 23^oC$ and using the commonly accepted value of the absorption coefficient of 30.4 $cm^{-1}atm^{-1}$ at the 10P(14) line of the $^{12}C^{16}O_2$ laser. For shorter time intervals (by changing the calibration gas mixture after a careful vacuum cleaning of the PA cell), the variation of the cell constant was smaller than

2%. The calibration also depends to some extent on the modulation waveform, since only the fundamental Fourier component of that waveform is resonant with, and hence significantly excites, the first longitudinal mode.

Using this PA cell and an optimized experimental arrangement we measured a cell responsivity R = 280 V cm/W. With the total responsivity of the four microphones $S_{M\,tot}$ = 80 mV/Pa (20 mV/Pa each) (Eq. 30, Part I), a cell constant C = 3500 Pa cm/W can be calculated (Eq. 28, Part I). A comparison of these PA cell parameters with other results reported in the literature is presented in Table 1. Different photoacoustic resonator designs such as longitudinal organ pipe resonators excited in the first longitudinal mode, closed longitudinal resonators excited in the second longitudinal mode, and cylindrical resonators excited in the first radial mode (Fig. 16) were used by various authors. As can be noticed from the table, the cell responsivity we obtained is one of the best values that have been reported up to now.

Authors	**Excitation mode**	**PA cell characteristics**	***R*** **(V cm/W)**	***C*** **(Pa cm/W)**
(Dumitras et al., 2007) - Our results	First longitudinal mode	L = 30 cm, f_0 = 564 Hz, 4 microphones, S_M = 80 mV/Pa, Q = 16.1	280	3500
(Crane, 1978)	Nonresonant operation	L = 20 cm, f = 33.3 Hz, 1 microphone	16.3	
(Gerlach & Amer, 1980)	First radial mode	6.54x15.56 cm², f_0 = 2.7 kHz, 1 microphone, S_M = 11mV/Pa + preamplif.x10, Q = 560	26.5	241
(Hubert, 1983)	Nonresonant operation	L = 20 cm, f = 695 Hz, 1 microphone	121[a]	
(Ryan et al., 1983)	First longitudinal mode	L = 30 cm, f_0 = 695 Hz, 1 microphone, Q = 17.4	56	
(Gandurin et al., 1986)	Nonresonant operation	L = 15 cm, 2r = 1.5 cm, 1 microphone, S_M = 50 mV/Pa	1-10	(20-200)[b]
(Bernegger & Sigrist, 1987)	Second longitudinal mode	L = 60 cm, f_0 = 555 Hz, 1 microphone, Q = 52		1990
(Sauren et al., 1989)	First longitudinal mode	L = 10 cm, f_0 = 1608 Hz, 1 microphone, S_M = 10 mV/Pa	(39)	3900
(Rooth et al., 1990)	First longitudinal mode	L = 30 cm, f_0 = 556 Hz, 4 microphones	114	
(Harren et al., 1990b)	First longitudinal mode	L = 30 cm, f_0 = 560 Hz, 4 microphones, S_M = 40 mV/Pa, Q = 16.4	(200)	5000
(Harren et al., 1990a)	First longitudinal mode	L = 30 cm, f_0 = 560 Hz, 4 microphones, S_M = 40 mV/Pa, Q = 20	(160)	4000
(Harren et al., 1990a)	First longitudinal mode (intracavity operation)	L = 10 cm, f_0 = 1653 Hz, 1 microphone, S_M = 10 mV/Pa, Q = 31.8	(37)	3700

Authors	Excitation mode	PA cell characteristics	*R* (V cm/W)	*C* (Pa cm/W)
(Meyer & Sigrist, 1990)	First radial mode	4.18x16 cm², f_0 = 2.65 kHz, 1 microphone, S_M = 12.5 mV/Pa, Q = 340	3.5	(280)
(Thöny & Sigrist, 1995)	Resonance in vicinity of the first radial mode	4.18x16 cm², f_0 = 2.86 kHz, 2 microphones, S_M = 25 mV/Pa, Q = 168	1.72	(69)
(Bijnen *et al*., 1996)	First longitudinal mode	L = 15 cm, f_0 = 1030 Hz, 1 microphone, S_M = 1000 mV/Pa, Q = 40	(2000)	2000
(Fink et al., 1996)	First longitudinal mode (intracavity operation)	f_0 = 1986 Hz, 1 microphone, S_M = 26 mV/Pa	(52)	2000
(Harren et al., 1997)	Second longitudinal mode	L = 45 cm, f_0 = 555 Hz, 1 microphone, S_M = 1000 mV/Pa, Q = 43	(1.64)	1640
(Harren et al., 1997)	First longitudinal mode	L = 10 cm, f_0 = 1600 Hz, 3 microphones, S_M = 60 mV/Pa, Q = 32	(270)	4500
(Henningsen & Melander, 1997)	Nonresonant operation, pulsed excitation	Cell volume = 1 cm³, f = 1600 Hz	1.45	
(Nägele & Sigrist, 2000)	First longitudinal mode in a multipass resonant PA cell	5x12 cm², f_0 = 1250 Hz, 16 microphones, S_M = 160 mV/Pa, Q = 70	260	(1625)
(Pushkarsky et al., 2002)	First longitudinal mode	f_0 = 1915 Hz, 1 microphone, S_M = 22 mV/Pa, Q = 49.7	(71.5)	3250[c]

[a] The value of 50 V cm/W reported for a rms signal of 162 mV was corrected for a peak-to-peak signal of 402 mV.
[b] In brackets are the values we deduced using the authors' specifications for microphone responsivity.
[c] These authors calculated the cell constant by using a PA signal $\sqrt{2}$ rms instead of a $2\sqrt{2}$ x rms signal; as a result, their cell constant (and responsivity) value is half the one we obtained by our methodology of calculus.

Table 1. Comparison of our results with different PA cells.

Based on the measured noises, background signals, and cell responsivity, all parameters characterizing the PA instrument can be evaluated (see Table 2). Some of them depend on the CO_2 laser and the PA cell, while others are determined by either the coherent acoustic background noise or the coherent photoacoustic background signal.

Several factors influence the lowest levels at which selected compounds can be detected by CO_2 laser spectroscopic techniques, within prescribed confidence limits, in a multicomponent mixture. These factors, some of which are interdependent, include (1) the sensitivity or minimum detectable absorptivity α_{min} (cm^{-1}) of the particular CO_2 laser detection technique

employed; (2) the absorption coefficients and spectral uniqueness of both the compounds of interest and interferences; (3) the total number of compounds that absorb within the wavelength regions of the CO_2 laser output; (4) the wavelengths and number of CO_2 laser lines used for monitoring; and (5) the output power of the laser at each of these lines when the photoacoustic technique is employed. The minimum concentrations of various vapors that can be detected under interference-free conditions by the CO_2 laser photoacoustic technique are given by the relationship $c_{min} = \alpha_{min}/\alpha(\lambda)$. Here α_{min} is the minimum detectable absorptivity value for the photoacoustic detection system in units of cm^{-1}, and $\alpha(\lambda)$ is the absorption coefficient in units of $cm^{-1}atm^{-1}$ of the vapor of interest at the CO_2 laser monitoring wavelength. In order to determine the concentrations of the various gas mixture components, it is necessary to know the absolute absorption coefficients for every gas component at the laser wavelengths. Our CO_2 laser photoacoustic system with a α_{min} value of $2.7x10^{-8}$ cm^{-1} should provide interference-free minimum detectable concentrations between 0.9 ppbV and 270 ppbV for vapors with usual absorption coefficients of 30-0.1 $cm^{-1}atm^{-1}$.

Parameter/units	**Value**
Resonance frequency, f_0 (Hz)	564
Quality factor[a], Q	16.1
Cell responsivity[b], R (V cm/W)	280
Microphone responsivity[c], S_M (V/Pa)	$4 \times 20x10^{-3} = 8x10^{-2}$
Cell constant[d], C (Pa cm/W)	$3.5x10^{3}$
Pressure amplitude response[e], p/P_L (Pa/W)	10^{-1}
Limiting sensitivity of the cell[f], S_{cell} (W cm^{-1})	$2.6x10^{-8}$
Limiting sensitivity of the system[g], S_{sys} (cm^{-1}) (at 4.4 W laser power)	$5.9x10^{-9}$
Limiting measurable concentration of ethylene[h], c_{lim} (ppbV)	0.2
Minimum measurable signal in nitrogen[i], V_{min} (μV) (root mean square)	12
Minimum detectable pressure amplitude[j], p_{min} (Pa)	$4.2x10^{-4}$
Minimum detectable concentration[k], c_{min} (ppbV)	0.89
Minimum detectable absorptivity[l], α_{min} (cm^{-1})	$2.7x10^{-8}$
Minimum detectable absorption cross-section per molecule[m], σ_{min} (cm^2)	$1.1x10^{-27}$
Cell sensitivity for 1 ppbV of C_2H_4 at 1 W of unchopped laser power[n], V_{ppb} (μV at 1 ppbV)	3.0

[a] This quality factor value corresponds to a full bandwidth at the 0.707 amplitude points of $\Delta f = f_0/Q \cong 35$ Hz

[b] The cell responsivity is the signal per unit power per unit absorption coefficient; in our case, the signal per unit power is 11.6 mV/4.0 W = $2.9x10^{-3}$ V/W (rms value) or $8.2x10^{-3}$ V/W (peak-to-peak value) for 0.96 ppmV of C_2H_4 (the absorption coefficient $\alpha^* = 30.4$ cm^{-1} atm^{-1} x $0.96x10^{-6}$ atm = $2.92x10^{-5}$ cm^{-1}, where $\alpha = 30.4$ cm^{-1} atm^{-1} is the absorption coefficient of C_2H_4 at 10P(14) line of the CO_2 laser), so that R = $8.2x10^{-3}$ V/W/$2.92x10^{-5}$ $cm^{-1} \cong 280$ V cm/W; the same responsivity was obtained with the etalon mixture of 10 ppmV of C_2H_4 in N_2: $R = 8.4x10^{-2}$ V/W/$3x10^{-4}$ $cm^{-1} \cong 280$ V cm/W

[c] The microphone responsivity is determined from the Knowles data-sheet for the microphone type 3033: 54 dB (≅500) attenuation at 564 Hz from 1 V/0.1 Pa, leading to $S_M \cong 20$ mV/Pa

[d] The cell constant is the pressure amplitude per unit absorption coefficient per unit power: $C = R/S_M$

[e] The pressure amplitude response per unit incident power for 1 ppmV of C_2H_4 is $p/P_L = C\alpha^*$

[f] The limiting sensitivity of the cell is $S_{cell} = 2\sqrt{2}\ V_N^{ac} / R$ (several authors, e.g., (Harren et al., 1990a) used the rms value of the voltage instead of its peak-to-peak value, resulting in a limiting sensitivity of the cell and of the system and the limiting measurable concentration of ethylene lower by a factor of 2.84; other authors, e.g., (Kosterev et al., 2005), used a parameter named "sensitivity to absorption",

defined as $D = \alpha_{\min}^{el} P_L / \sqrt{\Delta f} = S_{cell} / \sqrt{\Delta f}$, where $\alpha_{\min}^{el}$ is the absorption coefficient corresponding to the coherent acoustical background noise-equivalent signal V_N^{ac} , P_L is the laser excitation power, and Δf is the detection bandwidth).

[g] The limiting sensitivity of the system or the microphone noise-limited minimum detectable absorption coefficient (the equivalent bulk absorption coefficient in the gas) is $S_{sys} = S_{cell}/P_L$ (the minimum detectable absorption strength is defined as the strength that gives a SNR at the transducer output equal to one).

[h] The limiting sensitivity of the system gives a limiting measurable concentration of ethylene of $c_{lim} = S_{sys}/\alpha$.

[i] The minimum measurable signal in nitrogen, as determined by the coherent photoacoustical background signal, is $V_{min} = V_N^b$ (nitrogen) x P_L.

[j] The minimum detectable peak-to-peak pressure amplitude can be determined by dividing the minimum measurable signal in nitrogen by the responsivity of the microphone: $p_{min} = 2\sqrt{2}\ V_{min}/S_M$.

[k] The minimum measurable signal in nitrogen, limited by the synchronous background signal, gives a minimum detectable concentration $c_{min} = 2\sqrt{2}\ V_{min}/\alpha 2P_{meas}R$, where P_{meas} is the measured laser power after chopper: $P_L = 2P_{meas}$.

[l] The minimum detectable absorption coefficient or the equivalent absorption coefficient of C_2H_4 for a minimum detectable concentration (the absorption coefficient corresponding to the synchronous background signal) is $\alpha_{min} = c_{min}\alpha = 2\sqrt{2}\ V_N^b/R$ (or the ratio between the peak-to-peak value of the synchronous background signal and the cell responsivity).

[m] The minimum detectable absorption cross-section per molecule of ethylene determined by the synchronous background signal is the ratio between the equivalent absorption coefficient of C_2H_4 for minimum detectable concentration and the number of absorbing molecules per unit volume: $\sigma_{min} = \alpha_{min}/N_{tot}$, where N_{tot} is the number of absorbing molecules per cubic centimeter ($N_{tot} = 2.5\text{x}10^{19}$ cm^{-3} at 1013 mbar and 20^{o}C).

[n] Knowing the cell responsivity, we can determine the sensitivity of the photoacoustic cell (the rms voltage amplitude measured by the lock-in amplifier) to measure 1 ppb of a given gas at a given laser frequency with 1 W of unchopped laser power: $2\sqrt{2}\ V_{ppb} = \alpha P_L R c$ ($\alpha = 30.4$ cm^{-1} atm^{-1}, $P_L = 1$ W, $R = 280$ V cm/W, and $c = 10^{-9}$ atm).

Table 2. PA cell parameters.

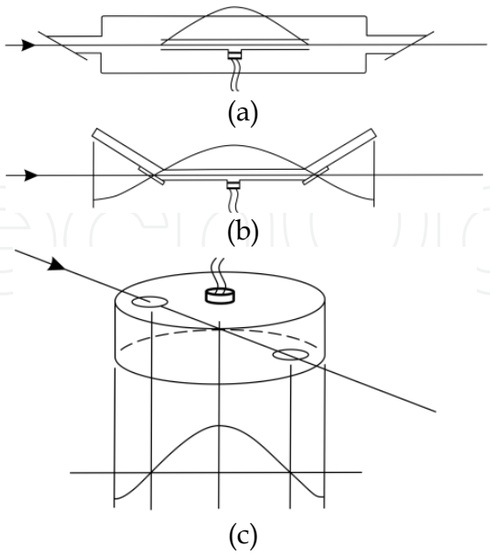

Fig. 16. Different photoacoustic resonator designs: (a) longitudinal organ pipe resonator, excited in the first longitudinal mode; (b) closed longitudinal resonator excited in the second longitudinal mode; (c) cylindrical resonator excited in the first radial mode.

A comparison of the results we obtained by using an extracavity PA cell and the experimental parameters measured using intracavity PA cells is given in Table 3. If we take into consideration only the parameters determined by the coherent acoustical background noise (SNR = 1), then the minimum detectable absorptivity S_{sys} (cm^{-1}) is much lower (1-2 orders of magnitude) in the intracavity arrangements due to the increased laser power. Unfortunately, only SNR is often considered in the literature, which yields an extrapolated detection limit that may be considerably too small. In reality, other background signals such as window absorption limit the ultimate sensitivity. These background signals must always be taken into consideration, as they can only be reduced, but not eliminated. In real PA instruments, the minimum measurable signal V_{min} is higher in extracavity PA cells (3 times in our case) and much higher in intracavity PA cells (hundreds or even thousands of times) than the coherent acoustic background noise V_N^{ac}. From this table it clearly follows that the best sensitivity is obtained with our extracavity PA instrument, with α_{min} (cm^{-1}) being better by one or two orders of magnitude than in intracavity arrangements.

Parameter	**Our results (Dumitras et al., 2007)**	**(Harren et al., 1990a)**	**(Fink et al., 1996)**
PA cell and CO_2 laser			
R (V cm/W)	280	37	52
$S_{M\,tot}$ (mV/Pa)	80	10	26
C (Pa cm/W)	3500	3700	2000
P_L (W)	4.4	100	40
p/P_L (Pa/W)	10^{-1}	$1.1x10^{-1}$	$6x10^{-2}$
Parameters determined by the coherent acoustic background noise (SNR = 1)			
V_N^{ac} (rms)[a] (μV)	2.6	0.5	0.81[b]
S_{cell} (W cm^{-1})	$2.6x10^{-8}$	$4.0x10^{-8}$ [c]	$4.4x10^{-8}$
S_{sys} (cm^{-1})	$5.9x10^{-9}$	$5.1x10^{-10}$ [d]	$1.1x10^{-9}$
c_{lim} (pptV)	200	17[e]	34
Parameters determined by the coherent photoacoustic background signal (SBR = 1)			
V_N^b (rms) (μV/W)	2.7	1.5	26
V_{min} (rms) (μV)	12	117[d]	1040
p_{min} (Pa)	$4.2x10^{-4}$	$3.3x10^{-2}$	$1.1x10^{-1}$
c_{min} (ppbV)	0.9	3.8	46
α_{min} (cm^{-1})	$2.7x10^{-8}$	$1.2x10^{-7}$	$1.4x10^{-6}$

[a] For a bandwidth of 1 Hz.
[b] The authors claim that they determined a coherent acoustical background noise of 0.1 μV, but their measured S_{sys} and c_{lim} correspond to V_N^{ac} = 0.81 μV.
[c] The value of S_{cell} = $1.4x10^{-8}$ cm^{-1}, as cited by the authors, was corrected for a peak-to-peak value of the coherent acoustical background noise.
[d] A factor of 0.78 was introduced either in the absorption coefficient of ethylene or in the intracavity laser power to compensate for the influence of saturation; the value of S_{sys} = $1.8x10^{-10}$ cm^{-1} claimed by the authors was corrected for a peak-to-peak value of the coherent acoustical background noise.
[e] The value of 6 pptV claimed by authors was corrected for a peak-to-peak value of the coherent acoustical background noise

Table 3. Comparison of our results (extracavity PA cell) with the experimental parameters determined with intracavity PA cells.

To keep the flow noise at a sufficiently low level, the flow must be in the laminar regime. Another practical requirement is the time response, which is determined by the gas sample exchange rate in the resonant cell. In addition, a delay occurs because the gas flows from the inlet to the resonant cell first through the acoustic filter. A response time of < 1 s and a delay of < 10 s may occur in the continuous flow mode. Taking into account the largest dimension and the limiting value of the Reynolds number ($Re \leq 2300$ for laminar flow), the flow velocity should not exceed 1.7 m/s. This value is far too large, since it would give a flow rate of 4.8 L/min (large gas consumption). As an operating value a flow rate of up to 0.5 L/min was used. With this value, the maximum flow velocity was about 15 cm/s, the Reynolds number $Re < 200$, and the calculated response time $\tau < 0.7$ s. The response time determined from the rise time of the PA signal is longer due to gas mixing in the buffer volumes of the cell. Nevertheless, the measured response times are below 10 s for nonadsorbing gases. Adsorption on the PA cell may increase the response time significantly. Note that the adsorption effect can be effectively reduced by using appropriate wall materials and higher wall temperatures. The adsorption effects can prevent accurate determination of the vapor pressure, since even with an *in situ* sample the vapor pressure will equilibrate between the rate of vapor emission and rate of plating out.

Let us consider the system to be a cell with constant volume. For an ideal gas, $dT/dE = (nC_v)^{-1}$, so that $dp/dE = R/(C_vV)$. Here T is the temperature, p is the pressure, E is the absorbed energy, n is the number of moles of the gas, C_v is the molar heat capacity at constant volume of the gas mixture, R is the gas constant, and V is the volume of the cell. For a real photoacoustic system the contents of the cell do not completely equilibrate at the modulation frequency; thus the above equations are a simplification. However, they do emphasize the basic constraints for maximizing the photoacoustic signal; (1) the gas mixture in the cell should have the lowest possible molar heat capacity, and (2) the effective volume of the cell should be as small as possible. The latter is also advantageous when the sample amount is limited. The ideal conditions for PA spectroscopy are a gas mixture consisting of a small amount of sample buffered in a large amount of a nonabsorbing gas with a low C_v, such as rare gases, inside a cell with the smallest possible volume. Since the laser beam has cylindrical symmetry, the best way to minimize the volume is to use a cylindrically symmetric cell with an internal diameter barely larger than the diameter of the laser beam.

Cylindrical cells, without additions, such as baffles, gas valves, sample fingers, or microphone tubes, and having a diameter of less than about 1/4 of wavelength, behave as simple pipes. Since the speed of sound is inversely proportional to the mass density of the gas (see Eq. 6, Part I), the frequency is lower for a more massive gas. The speed of sound is effectively independent of the total buffer gas pressure. Some works suggest that using the heavier noble gases as buffers increases the signal-to-noise level in acoustically resonant PA spectroscopy (Thomas III et al., 1978).

Davidson et al. (Davidson et al., 1990) investigated the importance of window noise and the role of acoustic baffles in photoacoustic spectroscopy. Small amounts of dirt or imperfections can cause heating at the windows and thus the production of a photoacoustic background signal. Window absorption is a major problem for intracavity photoacoustic spectroscopy because of the high light intensity inside the cavity. The signature of window noise is that it is laser frequency independent; its intensity tracks the intensity of the exciting radiation. This signal can actually mask the signal of interest (see spectrum D in Fig. 17). It was shown that the window noise should decrease with increasing modulation frequency

(Rosengren, 1975), which suggests that a relatively high modulation frequency is advantageous. The approach to this problem is to keep the windows as clean as possible and place acoustic baffles between the windows and the body of the sample cell where the microphones are mounted.

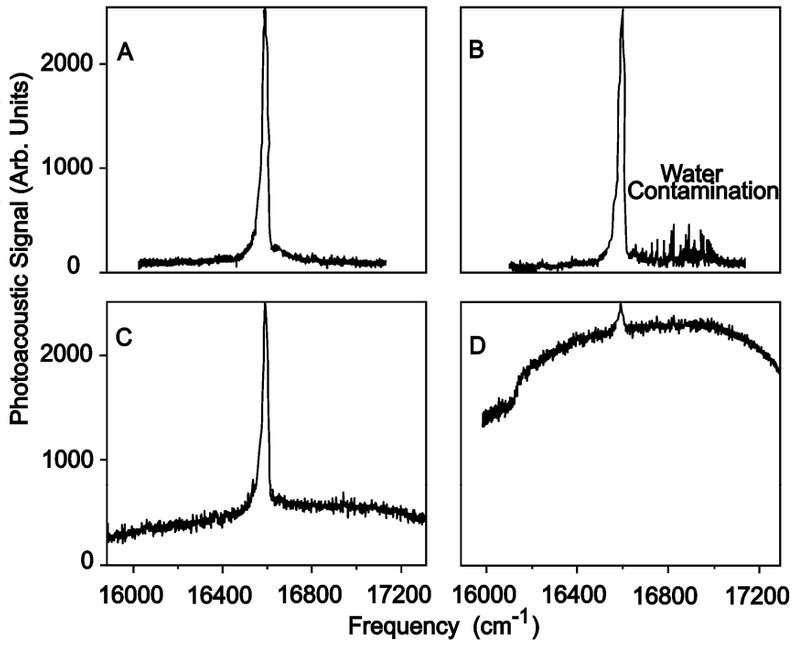

Fig. 17. Photoacoustic spectra: (A) clean windows on baffled cell; (B) clean windows on unbaffled cell; (C) dirty windows on baffled cell; (D) dirty windows on unbaffled cell (Davidson et al., 1990).

The acoustic baffles hinder the propagation of the window noise into the central region of the cell near the microphones. In an attempt to quantify the usefulness of the baffles, four spectra are shown in Fig. 17. These spectra illustrate the microphone signal versus laser frequency. For both the baffled and unbaffled cells, a longitudinal resonance frequency was used. From this figure it is immediately obvious how important it is to have clean windows. If the sample makes it difficult to keep the windows clean, a cell with baffles will perform much better than one without them. Even with clean windows, the baffles give a flatter base line.

The random noise level visible on the base lines of spectra A and B in Fig. 17 is probably due to a combination of the ambient lab noise, noise from the microphones, associated electronics, and the fluctuations of the laser itself. The ultimate limit of a microphone's sensitivity is set by the random thermal fluctuations in the sample and of the microphone diaphragm. In practice, the random fluctuations of the laser do not seem to be critical. Also, the combined electronic noise of the lock-in, preamplifier, and FET amplifier in the microphones totaled about 3 μV. This is at least a factor of 10 less than the noise level observed in the spectra. The noise that is visible in the spectra stems almost exclusively from thermal fluctuations and ambient lab noise. One of the major ambient noise sources is the mechanical chopper. In practice, this seems to set the detection limit. Acoustically isolating the chopper improves the noise, but replacing it with a nonmechanical modulator is better still, as it also speeds up modulation.

In an attempt to reduce the effects of microphone noise, the output of two microphones was summed in the low-noise preamplifier. Two microphones seem better than one when observing the noise level, but the difference is not as obvious in the spectra that were taken. However, the absolute signal level does increase with an increasing number of microphones; when the sample is weakly absorbing, more microphones are an advantage.

High isolation against window absorption may be obtained by introducing acoustic baffles between the windows and the resonator. However, the resonator also introduces additional noise. Pressure fluctuations from turbulence in the gas and acoustic flux reaching the resonator from the surroundings will be amplified along with the signal. Furthermore the amplification provided by a resonator is accompanied by an increased sensitivity to parameters which affect the resonance frequency, such as gas composition, temperature, and pressure.

Besides cleaning the cell windows, a very careful rinsing of the inner walls of the cell is also very important. If the inner of the cell is not properly cleaned before a measurement, a considerable drift of the photoacoustic background signal is observed if the gas flow is interrupted. This fact demonstrates that the desorption of IR-absorbing gases and vapors from the cell walls can make a large contribution to the background signal. That is why no measurement started until after the PA cell had been rinsed with pure nitrogen till the coherent photoacoustical background noise reached the minimum value of 2.7 μV/W.

To distinguish the gas absorption signal from other signals (e.g., from the walls, windows, or interfering gases), one has to switch the CO_2 laser to other laser lines. However, repositioning the laser beam to its original wavelength can change the configuration of the laser cavity (deviation in grating position, thermal drift) and result in irreproducible absorption signals if the operation is not carefully conducted. Using a CO_2 laser stabilized on the top of the gain curve ensures that both the laser frequency and output power are reestablished with high accuracy when the laser operation is changed from one line to another.

2.4 Gas handling system

Whenever monitoring is performed by flowing the gas mixture through a cell, a crucial question is whether the measured signal, which represents the trace gas concentration in the interaction region, also reflects the concentration at the source. On their way to the cell, the different components of a gas mixture may react with one another, form clusters or aerosols, and react with or be adsorbed on particles present, or on the sampling line and cell walls. Adsorption problems are particularly severe for polar molecules with large dipole moments, such as water and ammonia, but they can be reduced by a proper choice of materials.

The vacuum/gas handling system is an important element in these measurements owing to its role in ensuring PA cell and gas purity. The Teflon/stainless steel system can perform several functions without necessitating any disconnections. It can be used to pump out the cell, mix gases in the desired proportions, and monitor the total pressure of gases. Whenever possible, the PA cell was employed in the gas flow mode of operation to minimize any tendency for the vapor to stick to the cell walls and the effects of the subsequent outgassing of contaminants, which would otherwise lead to increasing background signals during an experimental run.

To design an efficient vacuum/gas handling system to be used in LPAS, one must make sure that the following operations can be carried out:

i. evacuation by the vacuum system of the entire gas handling system, including the PA cell, either totally or in different sections;
ii. controlled introduction of a gas or gas mixture either for rinsing the PA cell and the gas handling system with pure nitrogen or for calibrating the PA spectrometer with a certified gas mixture;
iii. pressure measurement in the PA cell and in different sections of the system;
iv. safe insertion in the gas handling system of a sample cuvette (usually made of Pyrex glass) or aluminum-coated plastic bag with the trace gas sample;
v. filtration of certain gases (carbon dioxide and water vapors), which interfere with the trace gas to be measured;
vi. controlled introduction of the trace gas to be measured from the sample cuvette or bag into the PA cell by a nonabsorbing gas (nitrogen or synthetic air) acting as carrier;
vii. controlled change of the sample and carrier gas flow rates within a broad range (10-1000 sccm);
viii. simultaneous measurement of two sample gases (e.g., ethylene and ammonia);
ix. quick monitoring of the trace gas concentration in the sample gas by ensuring a response time on the order of minutes or even seconds.

A vacuum/gas handling system to be used in PA experiments was designed and implemented based on these guidelines. The schematic of the gas handling chain is shown in Fig. 18, while a general view of the valves and distribution system is given in Fig. 19.

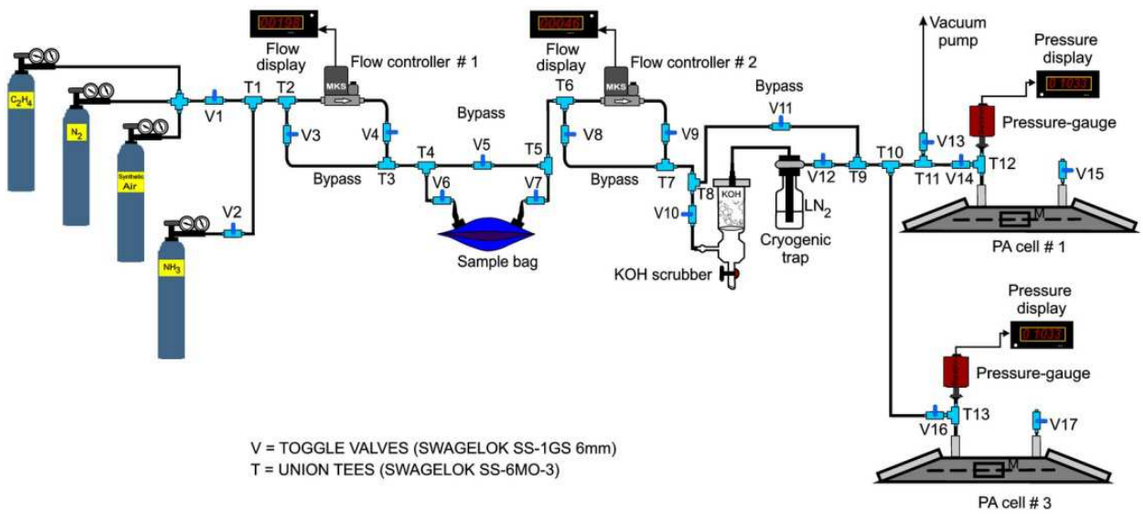

Fig. 18. Gas handling system.

Gas transport lines throughout the gas mixing station were made of Teflon (Swagelok PFA-T6M-1M-30M, 6 mm inner diameter and 1 mm wall thickness) to minimize adsorption and contamination. The toggle valves V1-V17 (Swagelok SS-1GS6mm) and union tees T1-T11 (Swagelok SS-6MO-3) were made of stainless steel. No valve grease was used. The PA cell gas inlet and outlet were connected to the gas handling system with Swagelok fittings (male connectors SS-6MO-1-2RT). Connections to the inlet and outlet valves of the PA cell were made via flexible Teflon tubing so as to minimize the coupling of mechanical vibrations to the PA cell. The flexible lines also make it possible to position the PA cell during optical alignment.

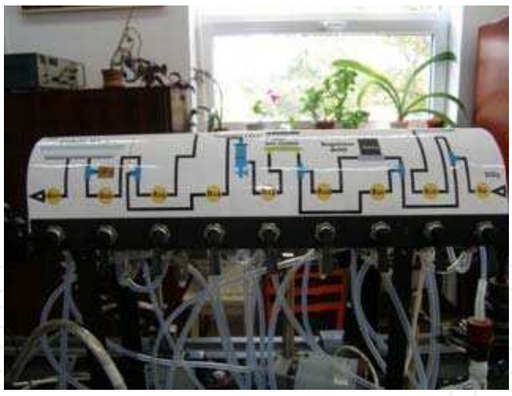

Fig. 19. General view of the gas mixing station.

The pressure of the gases added to the PA cell was determined by means of three Baratron pressure gauges (MKS Instruments, Inc.): 622A (0-1000 mbar), 122A (0-1000 mbar), and 122A (0-100 mbar), connected to a digital two-channel unit PDR-C-2C.

We use thermal mass flowmeters, or mass flow controllers (MFC), to deliver stable and known gas flows to the PA cell. The most critical processes will require flow measurement accuracies of 1% or better in the range 1000 to 10 sccm ($7x10^{-4}$ to $7x10^{-6}$ mol/sec; 1 sccm (at 0^oC) = $7.436x10^{-7}$ mol/sec). The digital MFCs sense the mass flow from the temperature difference between two temperature sensors in thermal contact with the gas stream and then process the information digitally with a microcontroller. The analog sensor output is amplified and digitized before it is sent to a microprocessor to compute the final control valve position. The gas flow in our gas handling system is adjusted by two gas flow controllers, MKS 1179A (0 - 1000 sccm) and MKS 2259CC (0 - 200 sccm), which are connected to a digital four-channel instrument MKS 247C.

By using an adequate scrubber for CO_2 filtration, the CO_2 interference problem can be resolved. The CO_2 trap must neither alter the ethylene concentration level, nor introduce new interfering gases. By using a CO_2 trap with a volume of 120 cm^3 filled with fresh KOH pellets, we succeeded to reduce the CO_2 content in the exhaled breath (mixt expiratory air collection) of a healthy nonsmoking young person from 3.4% (equivalent to an ethylene concentration of 2.35 ppmV) to 156 ppmV (equivalent to an ethylene concentration of 10.8 ppbV), that is a reduction factor of 218 (see Section 2.7).

The water vapors could be additionally filtered by a cryogenic trap filled with liquid nitrogen. Using a simple and small cryogenic trap, we demonstrated the negative influence in our experiments (Dumitras et al., 2008). The liquid nitrogen temperature -196^oC (77 K) is bellow the frozen point of the ethylene gas -169.2^oC (104 K), so the practical effects is just to frozen both water vapors and ethylene. Introducing in the flow a calibrated mixture of 1 ppm C_2H_4 in N_2, we observed after filling the cell at 1 atm pressure that the maximum ethylene concentration is only 51 ppb, diminished by a factor of 20 from the initial ethylene concentration. The level starts to increase suddenly at the point where we stopped the liquid nitrogen admission in the trap. In conclusion, a simple nitrogen trap is not suited for our experiments involving ethylene, but a special thermocontrolled trap can do the job, setting the working temperature below -78.5^oC (194.5K), the freezing point of CO_2, but above -169.2^oC (104 K), the freezing point of ethylene.

The following gases were used throughout the experiments:

- ethylene: Linde Gaz Romania, 0.96 ppmV (±5%) C_2H_4 diluted in nitrogen 5.0 (purity 99.999%) and 9.88 ppmV (±2%) C_2H_4 diluted in nitrogen 6.0 (purity 99.9999%)
- nitrogen: Linde Gaz Romania, nitrogen 5.0 (purity 99.999%) and 6.0 (purity 99.9999%);
- synthetic air: Linde Gaz Romania, 20% oxygen and 80% nitrogen (impurities: hydrocarbons max. 0.1 ppmV, nitrogen oxides max. 0.1 ppmV);
- carbon dioxide: Linde Gaz Romania, purity 99.95% (impurities: oils max. 1 ppmV);
- ammonia: Linde Gaz Romania, purity 99.98% and 9.66 ppmV (±5%) NH_3 diluted in nitrogen 6.0 (purity 99.9999%).

The flow rate was usually set at a low value of 30-100 sccm in all experiments in order to eliminate the acoustic noise of the gas flow, and all measurements were carried out with the PA cell at atmospheric pressure. Flow noise increases upwards of 10 L/h (167 sccm) were found to limit the minimum response time of the detector. The flow velocity minimizes the accumulation of the produced gases in the sampling cell. The carrier gas we used was either nitrogen or synthetic air, and its flow rate through the system was monitored by the calibrated flowmeter. Provision is made for bypassing the flowmeter with the gas mixture flow prior to a measurement to equilibrate the feedline surfaces. This ensures that the measured rise times are an exclusive function of the cell characteristics. A measurement is initiated by diverting the gas flow from the bypass through the flowmeter and PA cell and monitoring the photoacoustic signal rise that follows.

As far as the sampling procedure is concerned, we use an extractive method, based on the collection of trace gas samples by some type of container or collecting medium and subsequent analysis in the laboratory. A problem may arise at this point due to some alterations of the gas composition caused by adsorption and desorption processes on the inner surface of the collecting container. The breath samples we analyzed were obtained from volunteers who agreed to provide such samples at certain time intervals. The volunteers were asked to exhale into a sample bag with a normal exhalation flow rate. The breath samples were collected in 0.75-liter aluminum-coated bags (QuinTron, Milwaukee, Wisconsin, USA) equipped with valves that sealed them after filling (Fig. 20). The bags were inserted into the gas handling system, which ensured a better control by means of two independently adjusted flow controllers of the upstream pressure and the flow rate through the sample bag.

Fig. 20. Aluminum-coated plastic bag with sample gas.

The exhaled air is a heterogeneous gas. For a healthy individual, the first part of a exhaled breath, roughly 150 mL, consists of “dead-space” air from the upper airways (such as the

mouth and trachea), where air does not come into contact with the alveoli of the lungs. The following part of a breath, about 350 mL, is "alveolar" breath, which comes from the lungs, where gaseous exchange between the blood and breath air takes place. Dead space air can be interpreted as essential for the detection, and depends on the type of molecule detected from the breath test. For example, the dead-space is used to quantify the amount of the NO molecules. In the case of an asthmatic patient, if the airways are inflamed, a high-level of NO is released into the airways and into the dead-space air. But for volatile organic compounds (VOCs) exchanged between blood and alveolar air, the dead-space air is a "contaminant" diluting the concentrations of VOCs when breath air is collected. In terms of the origin of the collected breath gases, there are three basic collection approaches: 1. *upper airway collection* for NO test; this means that only dead-space gas is collected (it is only for the NO test); 2. *alveolar collection*; this means that pure alveolar gas is collected (for tests of other inorganic gases and VOCs); 3. *mixed expiratory collection*; this means that total breath air, including dead-space air and alveolar gas is collected (appropriate for tests of special gases and VOCs). Because the mixed expiratory collection method is easy to perform in spontaneously breathing subjects requiring no additional equipment, it has been most frequently used in practical applications. However, concentrations of endogenous substances in alveolar air are two to three times higher than those found in mixed expiratory samples, because there is no dilution by dead-space gas. Collection of breath air can be performed for a single breath or for collection of individual breathes over a certain period of time. If the sample is collected through a single breath, one has to be sure that this single breath is representative.

The rate of change in concentration of a species i in a flowing cell is given by:

$$\frac{\mathrm{d}C_i(t)}{\mathrm{d}t} = \frac{R_{flow}}{V}\left[F_i - C_i(t)\right], \tag{4}$$

where R_{flow} is the gas flow rate (liter/min or sccm), F_i is the feed concentration of species i, and V is the cell volume. This equation assumes that the adsorption rate of i is zero, and that gas mixing inside the cell is instantaneous. Integrating Eq. (4) with the initial condition that $C_i(0) = 0$ gives

$$C_i(t) = F_i\left[1 - exp\left(-R_{flow}t/V\right)\right], \tag{5}$$

and $\tau = V/R_{flow}$ is the renewal time constant.

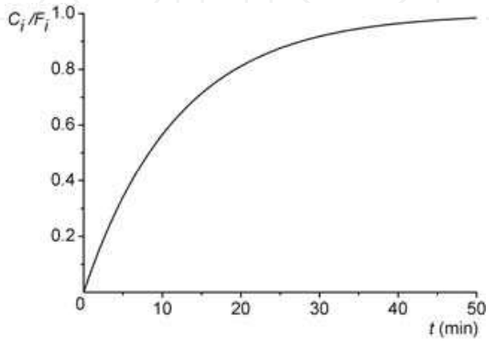

Fig. 21. Time response of the PA spectrometer for a gas flow rate of 100 sccm.

The solid line in Fig. 21 shows the rise time curve predicted by Eq. (5) for the experimental parameter values: V = 1200 cm^3 and R_{flow} = 100 sccm. The total renewal time of the gas content in the system (sampling cell, scrubber, and photoacoustic cell) is τ = 12 min ($1/e$ time). This τ value is small compared to the time response of certain biological samples (e.g., the C_2H_4 production of a single flower, 0.02-0.3 nL/g/h) (Harren et al., 1990b).

2.5 Data acquisition and processing

The acquisition and processing of the recorded data was done with Keithley TestPoint software. TestPoint data acquisition software provides a development environment in which data acquisition applications can be generated. A graphical editor is provided for creating a user interface, or "panel", which the user sees and interacts with as the application executes. A user panel is made of pictorial elements that represent such things as switches, variable controls, numerical, text and selection boxes, bar displays, graphs, and strip charts. In addition, an application editor is provided, which ensures some interactive means of specifying how the visual elements on the user panel interact with the data sources and processing functions to achieve application goals. TestPoint uses an automated textual description of the operations carried out by each user panel element.

We developed a modular software architecture aimed at controlling the experiments, collecting data, and preprocessing information. It helps automate the process of collecting and processing experimental results. The software controls the chopper frequency, transfers powermeter readings, normalizes data, and automatically stores files. It allows the user to set parameters such as the PA cell responsivity (a constant used to normalize raw data), gas absorption coefficient, number of averaged samples at every measurement point, sample acquisition rate, and total number of measurement points. This software interfaces the following instruments:

- lock-in amplifier;
- chopper;
- laser powermeter;
- gas flowmeter.

The software user interface allows the user to set or read input data and instantaneous values for the PA voltage (rms), average laser power after chopper, and trace gas concentration. Users may set experimental parameters for the PA cell responsivity and gas absorption coefficient. They are also provided with a text input to write a description of the experiments or take other notes. The user interface also provides data visualization (Fig. 22).

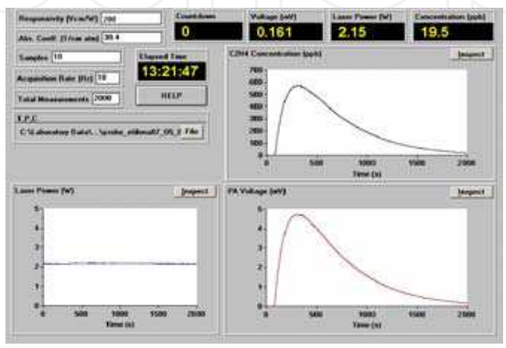

Fig. 22. Software user interface used to record trace gas concentrations.

The software user interface contains three panels which display in real time the following parameters: CO_2 laser power level; PA signal; and trace gas concentration. Another window (countdown) indicates the number of remaining measurement points.

All settings and properties are stored to disk from session to session. In addition, a file may be automatically generated when running an experiment, including: a) **Laser power** stores powermeter readings of power incident on the sample as a function of time; b) **PA signal** stores the instantaneous values of the PA signal measured by the lock-in amplifier as a function of time; c) **Trace gas concentration** stores the time evolution of the trace gas concentration for a given laser wavelength.

2.6 Low power vs. high power lasers

We designed and characterized two experimental set-ups with the PA cell in an external configuration: the first one with a low power CO_2 laser where the saturation effects are negligible, and a second one with a high power CO_2 laser where the saturation effects are important and have to be taken into consideration. We measured all relevant features and determined all quantities used in literature to compare our findings with the best results reported in the previous published papers. All measurements were done in nitrogen and ethylene with the 10P(14) line of a cw CO_2 laser. We succeeded to obtain a minimum detectable concentration better by more than a factor of 10 compared to the best results previously reported in the literature.

To investigate the possibility of using a high power laser in an extracavity configuration, we introduced in the experimental set-up a commercial CO_2 laser (Coherent GEM SELECT 50™ laser) with output power till 50 W and tunable on 73 different lines (Dumitras et al., 2010). When this laser is tuned on 10P(14) line, the maximum power delivered after chopper and focusing lens is 14.5 W.

To change the laser power inside the PA cell we tried either to modify the input power in the laser (RF power supply) or to introduce a beam splitter in the path of the laser beam. Unfortunately, both methods change significantly the beam path inside the PA cell, thus perturbing unacceptably the results of the measurements. The waveguide laser has a poor beam pointing because it has a short optical resonator and the variation of the transverse RF excitation modifies the laser gain profile.

The saturation effects at high laser power were investigated by using the method of truncation of a gaussian laser beam. This approach was possible because the laser beam is very close to a gaussian beam ($M^2 < 1.1$). The method consists in passing the beam through an aperture with known diameter (Fig. 23). To avoid deformations owing to heating, we used water cooled metallic diaphragms with diameters between 1.42 mm and 5.03 mm. All diaphragms were placed at a distance of 450 mm from the beam waist of the laser.

When a gaussian beam of radius w is truncated by an aperture of radius a (Fig. 24), the power transmitted through the aperture is $T = P(a)/P = 1 - \exp(-2a^2/w^2)$. When $2a = 2w$, $T \cong 86\%$, that is 86% of the laser power is transmitted through the aperture (this is known as 86% criterion). When $2a = \pi w$, $T \cong 99\%$, that is 99% of the laser power is transmitted through the aperture and we have the 99% criterion. This formula offers a possibility to measure precisely the diameter of the laser beam at the position of the diaphragm. By knowing the radius of the aperture (a) and by measuring the laser power before and after the aperture (P

and $P(a)$, respectively), we can determine immediately the radius of the laser beam (w). As it can be seen in Fig. 25, by using five different diaphragms, the resulting average diameter is $2w = (7.09 \pm 0.2)$ mm, with an error of less than 3%.

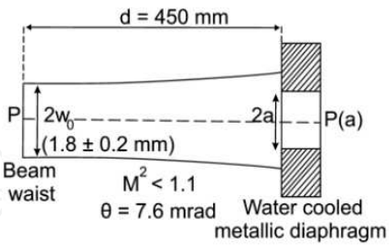

Fig. 23. Attenuation of a laser beam by a diaphragm.

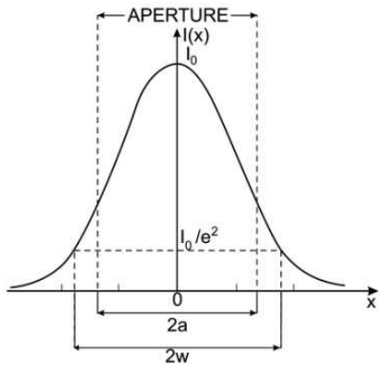

Fig. 24. Truncation of a gaussian laser beam.

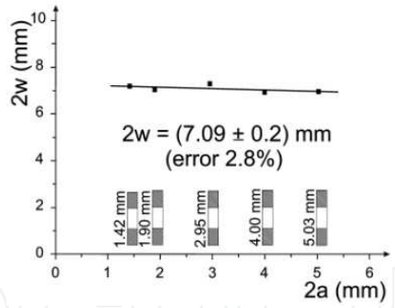

Fig. 25. Measurement of laser beam diameter by the method of truncation.

Figure 26 shows the attenuation of the laser beam when different diaphragms were placed in its path. The solid line is the theoretical curve given by the above equation. By introducing these five diaphragms, the laser power was varied between less than 2 W and near 10 W. In this way, we were able to investigate the laser power range from low power where saturation effects have no significance till high power where saturation effects manifest strongly.

We investigated the influence of saturation by measuring the dependence of the PA cell responsivity function on laser power (Fig. 27). From low laser power regime (under 2 W) where the saturation effects are not important till high power regime (14.5 W, no diaphragm), the PA cell responsivity decreases from 312 V cm/W till 52 V cm/W, that is by

a factor of 6. We can observe that the saturation effects manifest immediately as the laser power is increased more than 2 W. The cause of the saturation is that the collisional relaxation to de-excite the molecules cannot keep up with the excitation rate by the laser beam intensity. By increasing laser intensity, the excitation pumping rate of the molecules grows higher and a molecule is more likely to absorb a nearby photon before it relaxes to the ground state. So, as the number of molecules in the excited state increases, the number of molecules which can absorb laser radiation is reduced. That is why we introduced a supplementary scale in Fig. 27, representing the cell responsivity function on the intensity of the focused beam inside the PA cell. A thorough analysis of the laser beam propagation through the focusing lens and in the PA cell was done (Dumitras et al., 2007). For a lens with a focal length of 400 mm, we got in this case a beam diameter at beam waist of 0.89 mm. It can be remarked that saturation starts at laser intensities greater than 0.5 kW/cm^2. This result shows that saturation effects manifest even at low laser intensities. Previously, Harren et al. (Harren et al., 1990a) observed a strong saturation at a much higher intensity (200 kW/cm^2; the laser power was ten times higher and the beam area was ten times smaller than in our case at 13 W), when the PA cell was placed intracavity of a waveguide CO_2 laser. Our conclusion is that high power lasers could be used in PA systems, but saturation effects should be taken into consideration (by making a correlation between the PA cell responsivity and the working laser intensity, as in Fig. 27).

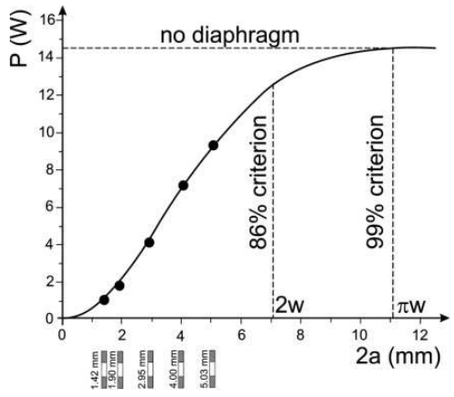

Fig. 26. Variation of laser power function on diaphragm aperture size.

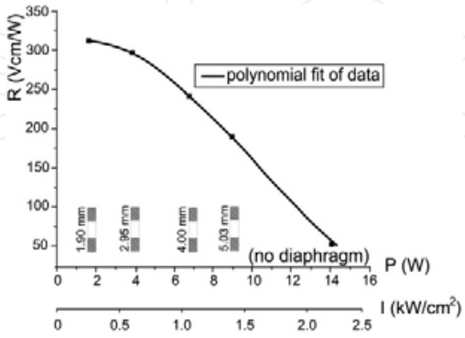

Fig. 27. Saturation effects measured as the dependence of the PA cell responsivity function on laser power and on laser intensity in the focal spot.

An important question is: what happens with the system noises when a diaphragm is introduced in the laser beam path? We proceeded to record the coherent PA background

signal on laser power (with and without a diaphragm) and the results are given in Fig. 28. The background signal is huge when a diaphragm is inserted into the system, being of more than 50 times higher than in the case that no diaphragm limits the laser beam. Truncation distorts the intensity pattern of the transmitted beam in both the near-field (Fresnel) and far-field (Fraunhofer) regions. The diffraction effects on an ideal gaussian beam of a sharp-edged circular aperture even as large as $2a = 2w$ (99% criterion) will cause near-field diffraction ripples with an intensity variation $\Delta I/I \cong \pm 17\%$ in the near field, along with a peak intensity reduction of ≅ 17% on axis in the far field (Siegman, 1986). In conclusion, the method of diaphragms used to measure the saturation effects is applicable, but in a laser PA system used in practice an aperture has never to be introduced.

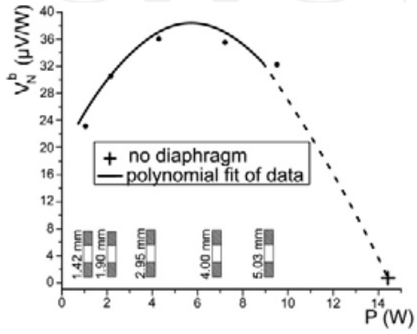

Fig. 28. Dependence of coherent PA background signal on laser power (with and without a diaphragm).

A comparison of low laser power vs. high laser power configurations is presented in Table 4. It seems resonable that high power lasers could be used in PA instruments provided that the saturation is considered and compensated.

Parameter	**Low power**	**High power**	**Factor**
Output laser power (W)	5.5	33	> 6.0
Average laser power (at cell exit) (W)	2.2	14.5	> 6.6
Coherent photoacoustic background signal (μV/W)*	2.7	0.7	< 4.0
Cell responsivity R (V cm/W)**	280	312	> 1.1
Signal saturation**	Small	Very high	> 6.0
Minimum detectable concentration c_{min} (ppbV)**	0.9	0.21	< 4.3
c_{min} (ppbV)***	0.04	0.009	
Minimum detectable absorptivity α_{min} (cm^{-1})**	$2.7x10^{-8}$	$0.64x10^{-8}$	< 4.3
Best value previously reported (Harren et al., 1990) (c_{min} = 3.8 ppbV)**	Better 4.2 x	Better 18 x	

Table 4. Comparison of low vs. high laser power configurations: 10P(14) laser line in N_2* (α = 0 $cm^{-1}atm^{-1}$), C_2H_4** (α = 30.4 $cm^{-1}atm^{-1}$), and SF_6*** (α = 686 $cm^{-1}atm^{-1}$).

To this date, the minimum detectable concentrations obtained by us in ethylene (0.9 ppbV with a low power laser and 0.21 ppbV with a high power laser) are the best values reported in the literature, improving this parameter by a factor of 4.2 in the first case and by a factor

of 18 in the second case. In a molecular gas with a high absorption coefficient (e.g. SF_6), the minimum detectable concentration could be as low as 9 pptV.

2.7 Removal of interfering gases

Interference of other absorbing substances may impair the theoretical detection limit in a multicomponent analysis of the real samples. Such interference may be caused by other molecular systems present in the environment or substances that are entrained by the carrier flux. If an interfering species is present in the environment, its effect can be minimized by either the introduction of scrubbers and cryogenic traps or the use of dual beam techniques using two photoacoustic (PA) cells.

The CO_2 laser spectral outputs occur in the wavelength region where a large number of compounds possess strong absorption features and where absorptive interferences from water vapors, carbon dioxide, and other major atmospheric gaseous components may influence the measurements.

The breath air is a mixture of nitrogen, oxygen, carbon dioxide, water, inert gases, and traces of VOCs (Table 5). The matrix elements in breath air vary widely from person to person, both qualitatively and quantitatively, particularly for VOCs. More than 1000 trace VOCs have been distinguished in human breath air, at concentrations from ppmV to pptV levels. Only a small number of VOCs are common to everyone, including isoprene, acetone, ethane, and methanol, which are products of core metabolic processes. In addition to these VOCs, exhaled NO, H_2, NH_3, and CO are related to health condition and can reflect a potential disease of the individual or a recent exposure to a drug or an environmental pollutant.

Component	**Inhaled air (%)**	**Exhaled air (%)**
Nitrogen	78.0	78.0
Oxygen	21.0	16.0
Carbon dioxide	0.04	3.0-5.0
Argon	0.93	1.0
Water	2.0	5.0-6.0
Other ammonia ethylene	0.01	 $250x10^{-9}$ (250 ppb) $6x10^{-9}$ (6 ppb)

Table 5. Concentration of different components in inhaled and exhaled air.

A healthy adult human has a respiratory rate of 12-15 breaths/min at rest, inspiring and expiring 6-8 L of air per minute. O_2 enters the blood and CO_2 is eliminated through the alveoli. When the end-tidal concentration of CO_2 in healthy persons is measured, a large change of CO_2 concentration is observed between the inhaled air (~ 0.04%) and the exhaled air (~ 4%). The exact amount of exhaled CO_2 varies according to the fitness, energy expenditure and diet of a particular person, with regular values of 3-5%. Due to this high concentration of carbon dioxide in the breath and because CO_2 laser lines are absorbed by this gas, it is necessary to remove most of the carbon dioxide from the exhaled air by introducing a scrubber filled with a chemical active agent, KOH in our case (Bratu et al., 2011).

Due to the exact coincidence of the CO_2 vibrational-rotational transitions with the CO_2 laser lines, carbon dioxide at high concentration in comparison with trace gases like C_2H_4 is

inevitably excited by CO_2 laser radiation and the related photoacoustic signal may exceed the trace signal by many orders of magnitude. The absorption coefficient increases strongly with temperature, but it is independent of the CO_2 concentration over a wide range. Ethylene can be excited by the 10P(14) line of the CO_2 laser, where the maximum absorption coefficient $\alpha(C_2H_4)$ has a value of 30.4 cm^{-1} atm^{-1} and ammonia by the 9R(30) line where $\alpha(NH_3)$ = 56 cm^{-1} atm^{-1} (Dumitras et al., 2011). A 4% concentration of CO_2 has an absorption strength comparable to 2760 ppbV of C_2H_4 (at the 10P(14) laser line, $\alpha(CO_2) = 2.1 \times 10^{-3}$ $atm^{-1}cm^{-1}$ and $c(C_2H_4) = c(CO_2)\alpha(CO_2)/\alpha(C_2H_4)$. This equivalent ethylene concentration was found also experimentally (see Fig. 29, measurement without trap). So, the photoacoustic signal is 100 times higher owing to exhaled carbon dioxide in comparison with the usual concentration of ethylene in exhaled air. Similarly, at the 9R(30) line of CO_2 laser, the same concentration of CO_2 has an absorption coefficient equal to that of 1500 ppbV of NH_3. This value is also considerably higher (6 times) compared to the real range of breath concentration which is situated approximately at 250 ppb for ammonia.

Water vapor exhibits a broad continuum with occasional weak lines in the frequency range of the CO_2 laser (for H_2O at the 10P (14) laser line, $\alpha(H_2O) = 2.85 \times 10^{-5}$ $atm^{-1}cm^{-1}$). The two dominant peaks are the absorption lines on 10R(20) and the most favorable one for ambient air measurement, the 10P(40) laser transition. A 5% concentration of H_2O has an absorption strength comparable to 46.9 ppbV of C_2H_4, that is the normal concentration of water in exhaled air has approximately the same influence in the photoacoustic signal as the normal concentration of ethylene.

Due to the additive character of the photoacoustic signal under normal pressure conditions, the presence of a large amount of water vapor and carbon dioxide impedes C_2H_4 detection in the low-concentration range (ppbV). Consequently, some means of selective spectral discrimination is required if ethylene is to be detected interference free in the matrix of absorbing gases. There are several ways to overcome this problem. One way is to remove CO_2 from the flowing sample by absorption on a KOH-based scrubber inserted between the sampling cell and the PA cell. Taking into account the nature of the specific chemical reactions involved in the CO_2 removal by KOH, a certain amount of water is also absorbed from the sample passing the scrubber. In this way, concentrations below 1 ppmV CO_2 (equivalent to a concentration of 0.07 ppbV of C_2H_4) can be achieved without influencing the C_2H_4 or NH_3 concentration.

Before entering the photoacoustic cell, the gas mixture passes through a KOH scrubber (Fig. 18), which retains most of the interfering carbon dioxide. The removal of CO_2 is limited to the absorbent surface of the pellets. Hence, the larger the surface area or the more porous the granular solid, the larger the capacity of the system to absorb CO_2. At the same time, the flow resistance varies inversely proportional to the particle size. Large particles offer less resistance, but have the disadvantage of providing a smaller total area for reaction. The granules of KOH that we used were typically Merck KOH pellets GR for analysis, with approximate dimensions of 10x7x2 mm. When residence time (time of contact between CO_2 and absorbent) is less than 1 second, CO_2 absorption capacity is greatly reduced, so we introduced flow controllers in order to ensure this pre-requisite.

Potassiun hydroxide is a caustic compound of strong alkaline chemical, dissolving readily in water, giving off much heat and forming a caustic solution. It is a white deliquescent solid in the form of pellets obtained by concentration of purified electrolytic potassium hydroxide

solution with very low chloride content. It reacts violently with acid and it is corrosive in moist air toward metals such as zinc, aluminum, tin and lead, forming a combustible, explosive gas. It absorbs rapidly carbon dioxide and water from air. Cautions must be taken when used because the inhaled dust is caustic and irritant, and touching skin or clothes could lead to less or more severe chemical burnings.

We have investigated the efficiency of the KOH scrubber using four recipients with different volumes (13 cm^3, 45 cm^3, 120 cm^3, and 213 cm^3, respectively), and we found out what type has to be used in order to reduce efficiently the amount of CO_2 from the exhaled air sample (Bratu et al., 2011). The KOH scrubber must neither change the ethylene concentration level, nor introduce new interfering gases. The measurements were made each time on the same person (healthy female, 30 years old) and with a new filling of KOH pellets. The gas from the sample bag was transferred into the PA cell at a controlled flow rate of 300 sccm (only for the 13 cm^3 trap) or 600 sccm, in order to ensure a sufficient time of flow in the scrubber column and to minimize any tendency for the vapor to stick to the cell walls or any other effects of internal outgassing of contaminants, which would otherwise lead to increase background signals during an experimental run. The typical resulting final pressure inside the PA cell was around 700 mbar and the corresponding responsivity was 170 cmV/W (see Fig. 3, Part I).

The experimental results without the KOH scrubber showed an equivalent ethylene absorption concentration of 2750 ppbV (with alveolar air collection) and 2350 ppbV (with mixt expiratory air collection), representing mainly the contribution of ethylene, carbon dioxide, water vapors and ammonia to the absorption of 10P(14) CO_2 laser line (Fig. 29). We tested the efficiency of traps filled with KOH and having different volumes (between 13 cm^3 and 213 cm^3) in removing CO_2 from exhaled air.

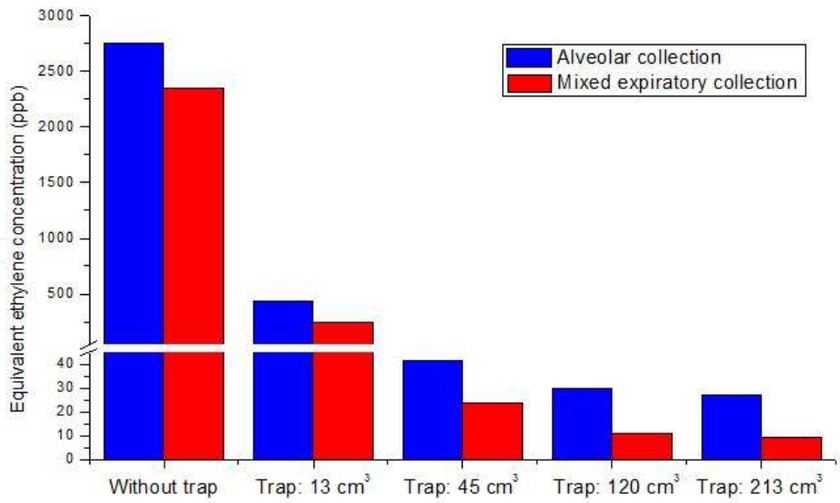

Fig. 29. Efficiency of KOH traps for CO_2 removal from exhaled air.

For the first measurement we used a trap with a small volume of 13 cm^3 of KOH scrubber, and we obtained a decrease of the PA signal down to 1-3 mV. The equivalent ethylene concentration was 435 ppb and 240 ppb, respectively (alveolar air collection vs. mixt expiratory air collection), indicating that the CO_2 concentration was reduced by factors of 6.3

and 9.8, respectively. Only in the case of this trap we observed a peculiar behaviour. Even if the laser power is constant, the PA signal and consequently the equivalent ethylene concentration increases in time after transfering the gas sample in PA cell. The increase of concentration starts from 50 ppbV and continues until it stabilizes at a level of 435/240 ppbV (after 10-15 minutes). It is known that C_2H_4 (28.05 g/mol molar mass) is lighter than CO_2 (44.0099 g/mol molar mass). Because of that, we can say that after passing the KOH scrubber, first C_2H_4 enters in the PA cell and then CO_2 when the trap is no longer effective. So, at the beginning, we measured only the C_2H_4 concentration and then CO_2 starts to strongly interfere in absorption. It is possible that due to the geometry of the cell, a longer time is required in order to attain the total homogeneity of the molecules inside the resonant tube of the cell, but this is not advantageous for repeated measurements.

Larger KOH traps proved to be more efficient in removal of CO_2 from the exhaled air. For the traps with volumes of 45 cm^3, 120 cm^3, and 213 cm^3, respectively, the measured equivalent ethylene concentrations were 41.5/23.6 ppbV, 30/10.8 ppbV, and 26.8/9.1 ppbV, respectively. For larger traps (120 cm^3 and 213 cm^3), approximately same results were obtained, indicating that most of the CO_2 was removed. By using larger traps, a higher transfer rate of the gas mixture in the PA cell is possible, doubling the flow rate to 600 sccm.

For the two largest volumes, we succeeded to reduce the CO_2 content from the exhaled air at a level influencing no more the C_2H_4 and NH_3 concentration values, fact proved by the constant evolution in time of all parameters. Therefore, the trap is effective only for a enough large amount of KOH pellets. We found that a minimum volume of 120 cm^3 of KOH scrubber and a transfer rate of 600 sccm were optimum to insure the required efficiency.

Analyzing the four cases when we inserted the scrubber, the dependence between the removed content of CO_2 and the used KOH quantity proved to be nonlinear, as one could expect. If we consider the content of the sample totally free of CO_2 after passing through the 213 cm^3 and 120 cm^3 KOH traps, we calculated a residual content of CO_2 in alveolar collection of 0.58% (5800 ppm) for the 13 cm^3 trap and of 0.016% (160 ppm) for the 45 cm^3 trap (less than half of the CO_2 concentration in the inhaled air).

We measured also the efficiency of the KOH scrubber when it is used for multiple measurements (Fig. 30). A clear saturation effect is evident: the KOH scrubber is not anymore efficient when the same fill is used for multiple runs (it cannot absorb completely the CO_2 from the gas mixture). In the case of alveolar collection, the equivalent ethylene concentration increases by 2.3 times for the second run, by 2.6 times for the third run and by 3.4 times for the fourth run. When we measured the mixed expiratory collection, this saturation effect is even larger: the equivalent ethylene concentration increases by 2.4 times for the second run, by 8.5 times for the third run and by 20.2 times for the fourth run. The conclusion is that a new fill of KOH scrubber must be introduced after each measurement.

The lungs and airways are always moist, and inspired gas is rapidly saturated with water vapor in the upper segments of the respiratory system. The temperature in the airways and lungs is most identical with deep body temperature (approximately 37^{o}C); at this temperature water vapor has a partial pressure of 47 torr (~6.2%). The increased saturation found at the third and fourth run for mixed expiratory collection is explained by a higher quantity of water vapors in exhaled breath (originating both from lungs and from upper segments of the respiratory system).

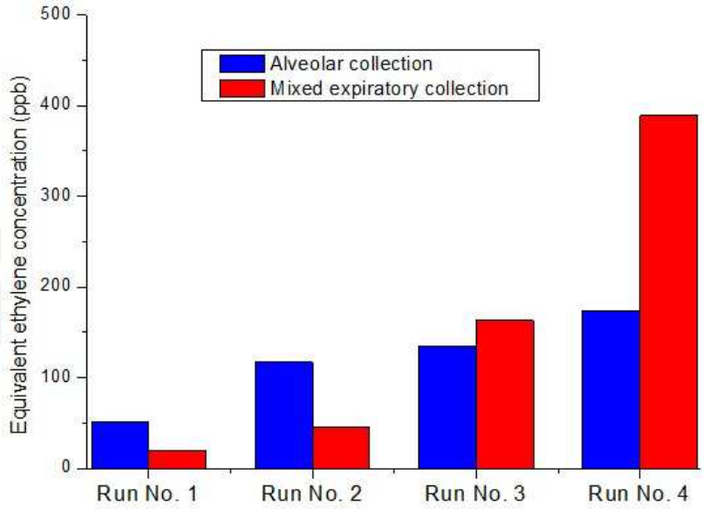

Fig. 30. Decrease of KOH trap efficiency when the same fill was used for multiple measurements.

The nonlinearity of the CO_2 removal could be explained by the mechanism of the chemical reactions. First, the CO_2 combines with the water vapors present in the exhaled air in the form of carbonic acid:

$$CO_2 + H_2O \Rightarrow H_2CO_3. \quad (6)$$

Further, the last one combines with the KOH, creating potassium carbonate and water, and releasing a small amount of heat:

$$H_2CO_3 + 2KOH \Rightarrow K_2CO_3 + 2H_2O + \text{Energy}. \quad (7)$$

In the same time, K_2CO_3 is a highly hygroscopic compound with a retaining capacity of 0.2 g H_2O/1 g K_2CO_3, so the generated water will be only partially returned in the circuit.

The water is of high importance in limiting the rate of CO_2 absorption. High CO_2 concentrations entering the KOH absorber generates large quantities of water, because the reaction (7) is producing water. We know that the absorption rate is greater thanks to the film of moisture coating the pellets, but the same film impedes the access to the active potassium hydroxide pellet volume. More dedicated studies should be made in order to establish the moisture content for an optimum rate of absorption.

In conclusion, we determined experimentally that in the process of CO_2 removal from the breath air samples, a quantity of minimum 120 cm^3 KOH pellets should be used for a sampling bag of 750 mL in order to keep the detection of ethylene and ammonia traces free of CO_2 interference. It should be mentioned that this volume of 120 cm^3 must be reconsidered for sample bags with a greater volume (> 750 mL) or when the gas transfer rate from the bag to the PA cell is larger (> 600 sccm).

2.8 Recipe for an optimum PA system

Based on our experience, we summarize a list of actions to obtain a minimum detectable concentration (c_{min}) as low as possible (Dumitras et al., 2010):

a. Increase the cell constant, C:
- choose resonant operation of the PA cell (design the PA cell as an acoustic resonance chamber and modulate the laser beam at a frequency which coincides with one of the natural resonant acoustic frequencies of the chamber); in this case, the signal is amplified by the quality factor, Q;
- to increase the quality factor, minimize the energy lost over one period by different dissipation processes (surface losses and volume losses); radiation losses through openings can be reduced by terminating the cavity resonator at the openings with acoustic band-stop filters (buffer volumes);
- maintain the chopper frequency close to the top of the resonance curve (a signal reduction less than 2% is obtained if $\Delta T \leq 4^{o}C$);
- in a longitudinally excited resonator use a pipe with a large length ($C \propto L^{1/2}$) and a small diameter ($C \propto r^{-1}$).

b. Increase the microphone responsivity:
- by a higher individual microphone responsivity and/or by an increased number of microphones connected in series.

c. Minimize the electrical noise, V_N^e :
- use state-of-the-art lock-in amplifiers;
- use longer time averaging ($V_N^e \propto \tau^{-1/2}$).

d. Minimize the coherent acoustic background noise, V_N^{ac} (caused by the modulation process):
- use thick detector and tube walls;
- use small flow rates;
- mount the cell and the chopper in separate sound insulating boxes.

e. Minimize the coherent PA background signal, V_N^b :
- use high quality Brewster windows for PA cell (low absorption materials and best possible polished surfaces);
- adjust the windows of the PA cell at Brewster angle and respect the polarization angle of the laser beam;
- place the PA cell windows at the nodes of the mode being excited;
- introduce buffer volumes at both ends of the cell;
- align the laser beam such as to avoid wall interactions;
- do not use tight focused beams to avoid saturation effects.

f. Avoid interference with other absorbing substances:
- to remove CO_2 and H_2O from the flowing sample insert a KOH - based scrubber and a cryogenic trap, respectively, between the sampling cell and the PA cell;
- use multicomponent analysis of the real atmosphere (the minimum number of measurements at different laser wavelengths must be equal to at least the number of unknown trace gases);
- use the phase information of the PA response to suppress the CO_2 signal (a high concentration of CO_2 yields a phase shift of the signal with respect to the acoustic signal of ethylene).

g. Increase the laser power while maintaining the noises at lower values:
- increase the laser power either in extracavity configuration (higher output power) or in intracavity configuration (smaller cavity transmission coefficient);
- maintain all noises and especially the PA background signal at as low as possible values;
- avoid any aperture in the path of the laser beam;
- consider the saturation effects in PA cell responsivity.

The recipe presented above applied on an extracavity laser PA configuration allowed us to achieve one of the most sensitive PA system with a detection limit of $2.7x10^{-8}$ cm^{-1} for a low power laser or even $0.64x10^{-8}$ cm^{-1} for a high power laser. In this way, the method based on laser photoacoustic spectroscopy became a powerful tool for measurement of trace gases (Dumitras et al., 1996a).

3. Applications

3.1 Measurement of absorption coefficients

We have measured precisely the absorption coefficients of ethylene (Dumitras et al., 2007) and ammonia (Dumitras et al., 2011) at CO_2 laser wavelengths.

The ethylene absorption coefficients for various CO_2 laser transitions have been measured in various experiments. Discrepancies as high as ~15% have been found in the absolute IR values observed at many laser transitions. Such discrepancies are typical of many other gases and are partially associated with the difficulty of producing proper gas samples with known concentration levels. Unfortunately, large discrepancies are also found between measurements of the relative spectral signatures (the ratio between absorption coefficients at different wavelengths). Knowledge of the relative spectral signatures rather than absolute ones is sufficient for trace gas identification. We also note that it is rather problematic to obtain highly accurate measurements of the absolute values of the absorption coefficients of gases using the photoacoustic effect. The reason for this is the need of an absolute calibration of the cell. The calibrations cited in the literature are all based on *a priori* knowledge of the absorption coefficient of a gas at some selected wavelength. However, in all cases the absorption coefficient was actually known only to a few percent.

Photoacoustics is emerging as a standard technique for measuring extremely low absorptions independent of the path length and offers a degree of parameter control that cannot be attained by other methods. Radiation absorption by the gas creates a pressure signal which is sensed by the microphone. The resulting signal, processed by a phase sensitive detector, is directly proportional to the absorption coefficient and laser power (or laser power absorbed per unit volume). The sensitivity of the technique is such that absorptions of $<10^{-7}$ cm^{-1} can be measured over path lengths of a few tens of centimeters. The small volume of the chamber makes it possible to accurately control the gas parameters, and the system can be operated with static fills or in continuous gas flow mode.

The set of values of the absorption coefficients α, for all laser wavelengths, for a particular gas or vapor and at a common concentration is called the optoacoustic absorption spectrum or signature and is unique to a combination of vapor and laser. These signatures or "fingerprints" are absolute entities, unique only to the laser frequency and species, which provide the specifics of instrument performance in terms of detection limit and interference rejection (Cristescu et al., 2000b).

To improve the measurement of ethylene absorption coefficients, a special procedure was followed. Prior to each run, the gas mixture was flowed at 100 sccm for several minutes to stabilize the boundary layer on the cell walls, since a certain amount of adsorption would occur and possibly influence background signals; after this conditioning period, the cell was closed off and used in measurement. For every gas fill with 0.96 ppmV ethylene buffered in pure nitrogen, the responsivity of the cell was determined supposing an absorption

coefficient of 30.4 $cm^{-1}atm^{-1}$ at 10P(14) laser transition. After measurements at all laser lines, the cell responsivity was checked again, to eliminate any possibility of gas desorption during the measurement. The partial pressure of ethylene was enough to have significant PA signals for all laser lines and low enough to be far away from the saturation regime (observations were only made at a C_2H_4 concentration of 100 ppmV). The α values at each laser line were obtained from Eq. (29, Part I) using the measured PA signal and laser power (the cell responsivity and ethylene concentration were known). An average over several independent measurements at each line was used to improve the overall accuracy of the results. The values to be presented are thought to be the best published to date.

The absolute magnitudes of the absorption coefficients were calculated as mean values of several independent measurements. An absorption coefficient corresponding to each CO_2 laser transition was determined from two sets of 50 different measurements. Every set of measurements was initiated by the frequency stabilization of a given line of the CO_2 laser. From one set of measurements to another, the closed loop of the frequency stabilization circuit was interrupted, the laser was tuned again to the top of the gain curve, and then the frequency stabilization was set and checked by watching the long term stability. Inside one set, 50 independent measurements were made at a rate of one per second to assess reproducibility. From one measurement to the next, the error measurement of the absorption coefficient was calculated as the ratio between the maximum difference (maximum value minus minimum value) and the average value. The final value of the ethylene absorption coefficient is given by the arithmetic mean of the two sets of measurements, while the absorption coefficient error is chosen as the larger value of the two sets. The same procedure was applied for every absorption coefficient of ethylene.

To measure the absorption coefficients of ethylene, the software user interface was modified to allow that the laser power, PA signal, and calculated absorption coefficients function on time (or number of measurements) be recorded on different panels.

The results of our measurements for ethylene are given in Fig. 31. Because of the large spacing between laser transitions (1.2-2 cm^{-1} apart), strong differences of absorption occur. Our results are compared to those of Brewer *et al*. (Brewer et al., 1982) that were also obtained by a photoacoustic method. The difference between the two spectral patterns suggests problems in the measurement techniques (for example, frequency deviation from the laser line center, gas calibration, system purity, linearity, precision) and/or data analysis. The different temperatures and atmospheric pressures at which the measurements were made cannot account for the discrepancies, because Persson *et al*. (Persson et al., 1980) measured a change in absorption coefficient of only 5% at the 10P(14) line for a temperature change of 30°C (negative temperature coefficient), while the changes caused by a pressure difference of 40 Torr are <5% for all CO_2 laser wavelengths.

The random coincidence between the emission and absorption lines will be such that some laser lines will lie close to the centers of the absorbing lines and others will be far away in the wings. The result is a spectral representation unique to that molecule. As a consequence of the superposition of different pressure-broadened C_2H_4 transitions (ν_7 vibration), a strong absorption is obtained at the 10P(14) laser line (absorption coefficient of 30.4 $cm^{-1}atm^{-1}$ at 949.479 cm^{-1}). C_2H_4 has weaker absorption coefficients at the 10P(12) and 10P(16) CO_2 laser transitions (4.36 $cm^{-1}atm^{-1}$ at 951.192 cm^{-1} and 5.10 $cm^{-1}atm^{-1}$ at 947.742 cm^{-1}, respectively). Also, in Fig. 31 ethylene is seen to possess moderately strong absorption profiles within the 9.4-μm band.

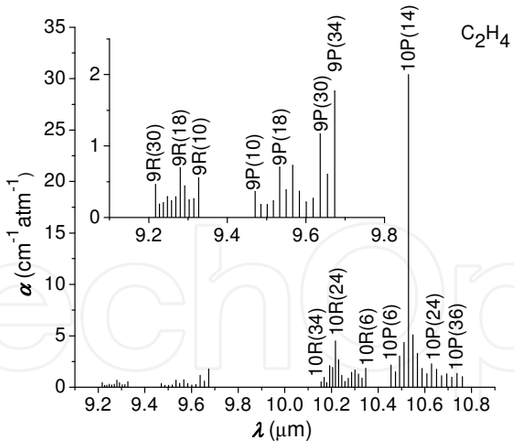

Fig. 31. Absorption coefficients of ethylene at CO_2 laser wavelengths. The inset shows an enlarged view of the measurements for the 9-μm band.

There is general agreement with the results of Brewer et al. (Brewer et al., 1982) for the 00^01-10^00 band. The difference between our results and those obtained by the above mentioned authors is less than 10% for the majority of the investigated lines while only for five lines the discrepancy is higher, between 10% and 20%. By contrast, the values determined in the present work are consistently higher in the 00^01-02^00 band. The difference is larger by 10-50% for the P branch, while our values in the R branch are higher by a factor of 1.5-5.5 (the largest discrepancies are recorded for the 9R(28), 9R(30), and 9R(22) laser lines).

The present work was carried out using a methodology which gave the best possible control over the ethylene partial pressure and background signals. The background levels and calibration of the PA cell were checked before and after every experimental run. The present study is considered reliable, particularly in view of the careful attention that was paid to controlling the gas composition and noise signals. No apparent fault could be found with either the apparatus or methodology that would account for the discrepancy by factors of 2-5 from other reported data in the case of the CO_2 laser 9R lines.

For the measurement of the absorption coefficients of ammonia (Dumitras et al., 2011), the software user interface allows to record the laser power, the PA signal and the calculated absorption coefficients on different panels**.** The evolution in time of the measurement of the absorption coefficients can also be displayed.

The gas mixture was flowed at 100 sccm for several minutes to stabilize the boundary layer on the cell walls, since a certain amount of adsorption would occur and possibly influence background signals; after this conditioning period, the cell was closed off and used in measurement. For every gas fill with 10 ppm ammonia buffered in pure nitrogen, the responsivity of the cell was determined supposing an absorption coefficient of 57.12 $cm^{-1}atm^{-1}$ at 9R(30) laser transition. This is in accordance both to the measurements reported by Brewer & Bruce (Brewer & Bruce, 1978) and by our tests, when the responsivity of the PA system was checked by measuring the well known absorption coefficient of ethylene at 10P(14) line of the CO_2 laser. After measurements at all laser lines, the cell responsivity was checked again, to eliminate any possibility of gas desorption during the measurement. The α values at each laser line were obtained by using the measured PA signal and laser power and by knowing precisely the ammonia concentration (10.6 ppm) and the responsivity of the

PA cell (312 V cm/W for high power laser). An average over several independent measurements at each line was used to improve the overall accuracy of the results.

The results of our measurements for ammonia are given in Fig. 32. The experimental results show a spectral representation unique to the ammonia molecule. As it can be seen from Fig. 32, ammonia has weaker absorption coefficients at other CO_2 laser transitions; some other significant values for the absorption coefficient were found for 9R and 9P bands: 9R(16) - α = 11.29 $cm^{-1}atm^{-1}$ (error ± 1.4%), 9P(20) - α = 2.10 $cm^{-1}atm^{-1}$ (error ± 2%) and 9P(34) - α = 3.99 $cm^{-1}atm^{-1}$ (error ± 0.62%). In the 10R band the measurements gave: 10R(14) - α = 6.17 $cm^{-1}atm^{-1}$ (error ± 1.5%), 10R(8) - α = 20.08 $cm^{-1}atm^{-1}$ (error ± 1.3%), 10R(6) - α = 26.2 $cm^{-1}atm^{-1}$ (error ± 1.7%), and for the 10P band: 10P(32) - α = 12.45 $cm^{-1}atm^{-1}$ (error ± 2.9%), 10P(34) - α = 14.07 $cm^{-1}atm^{-1}$ (error ± 0.48%) and 10P(36) - α = 7.39 $cm^{-1}atm^{-1}$ (error ± 0.83%). Compared to the other values reported previously in the literature (Brewer & Bruce, 1978), our measurements indicate a general good agreement.

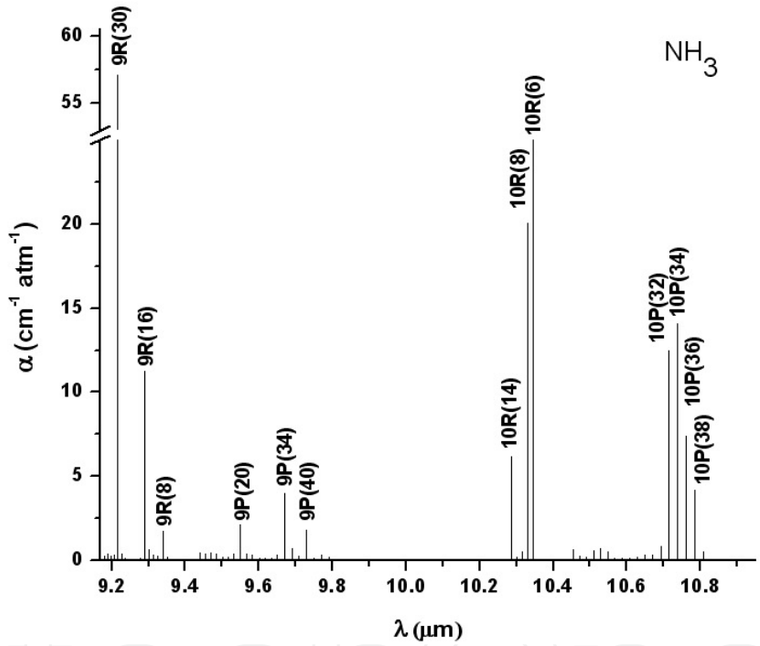

Fig. 32. Absorption coefficients of ammonia at CO_2 laser wavelengths.

3.2 Applications in plant physiology

Ethylene acts as a vegetal hormone produced by all plant tissues. It is transported by diffusion through plant tissues and increases the plasmatic membrane permeability. It has multiple effects on the cell metabolism: increases the oxidative processes, the transport inside the cells and the biodegradation of the organic acids and chlorophyll. Ethylene plays a major role in many metabolic processes: seed and bud dormancy, seed germination promotion, roots induction, development of plantlets (inhibitor of elongation and promotion of lateral shoots), grown promotion, leaf expansion, epinasty (downward curvature of leaves due to the growth of cells on the upper side of the petiole), flowering, wilting of flowers, fruit ripening (ethylene induces some biochemical modifications which produce polyalcohols, hydrocarbons and different oxygenated combinations responsible for the taste, aroma and

texture of the fruit), aging and senescence of leaves and flowers and finally, the abscission of leaves and fruits (Cristescu et al., 1998; Cristescu et al., 1999; Dumitras et al., 2004).

The ethylene biosynthesis process in plants follows the MSAE pathway: L-methionine (amino acid) – SAM (S-adenosyl methionine) – ACC (aminocyclopropane-1-carboxylic acid) – C_2H_4. Ethylene, or its precursor ACC, stimulates seed germination of many species at concentrations as low as 0.2 ppb. During germination, a complex cross-talking between several plant hormones exists.

Tomato is an useful model plant for studying ethylene action. Three tomato mutants altered in ripening process affects different steps in ethylene synthesis and perception, resulting in a delay of fruit maturation and pigmentation: Never ripe (*Nr*) is mutated in an ethylene receptor and exhibits delayed and incomplete fruit maturation; ripening inhibitor (*rin*) is a delayed gene that causes the block of ripening before the respiratory burst; and non ripening (*nor*) shows pleiotropic effects analogue to *rin.* The aim of our study was to investigate the ethylene emission during seed germination of these 3 mutants, correlation with their germination ability and analysis of ethylene role on the loss of germinability during seed senescence.

The ethylene production per seed measured during seed germination and seedling elongation is presented in Fig. 33. In these genes, ethylene influences not only fruit ripening, but also the seed germination. The germination index and the percentage of germination of the 5-years-old seeds of the mutants are higher in respect to the control (Ny – New Yorker), in spite of the lower ethylene production of germinating seeds. Conversely to other species, in 5-years-old tomato seeds an inverse correlation between ethylene production and percentage of germination exists. During seed senescence, ethylene accumulation occurs and some processes, triggered during germination, result altered. Further analysis is required to clarify the interaction between ethylene and other hormones like auxin, ABA and cytochinin.

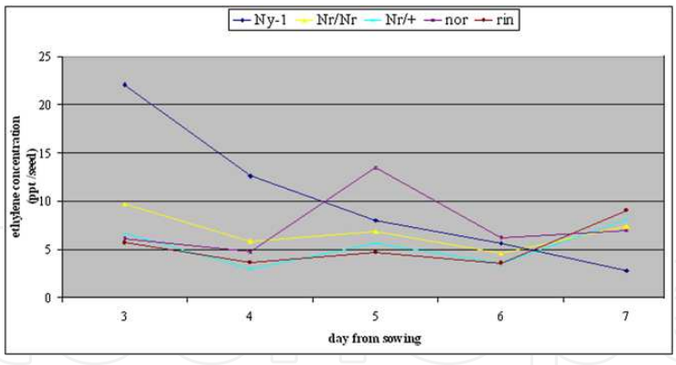

Fig. 33. Ethylene production (ppt/seed) measured during seed germination and seedling elongation.

Climacteric fruits show a respiratory rise during ripening (tomato, pear, fig, mango, banana), while others belong to nonclimacteric fruits (cherry, strawberry, lemon). Fruit ripening (yellowing, softening, respiration, autocatalytic ethylene production) and abscission are regulated by ethylene. During ripening, tomatoes show a strong increase in ethylene production coinciding with the climacteric rise in respiration (CO_2 production). Ethylene is also involved in the postmaturation processes, playing an important role in fruit ripening. Storage and shipping of fruits in terms of wounding effects, temperature, composition of atmospheric gases, postharvest pathogens or seal-packing conditions are

important factors to establish the optimal environment necessary for their long term conservation. The aim of our experiments was to monitor the ethylene emission in plants and fruits at low temperature, together with the effect of the temperature at different ripening stages (important for optimization of different stages in agricultural procedures) and to study the effects of mechanical wounding of fruits.

Ethylene emission was monitored from plantlets at different temperatures and it saturates after about 20 min (Lai et al., 2003). The temperature effect is evident in the emission intensity, which increases almost a factor four from 15° to 25°C. There is a remarkable decrease in the lag time for the gas emission at the optimum temperature for biosynthesis of ethylene (25°C). At temperatures lower than 22°C, this lag time is about 6 min, while drops to less than 2 min at 25°C. Temperature does not influence the ethylene emission of immature fruits (0.004 ppb/g and 0.005 ppb/g for 15°C and 25°C, respectively), while it becomes important when the ripening process is triggered in a maturated fruit (0.012 ppb/g and 1.56 ppb/g for 15°C and 25°C, respectively). The same result is obtained for plantlets. Temperature is important for ACC oxidase activity (decreased at low temperatures). Mechanical wounding exerts its effect at the step where SAM is converted to ACC, the direct precursor of ethylene; this step, regulated by the enzyme ACC synthase is rate limiting in the cascade of events leading to an increase of ethylene production.

3.3 Investigation of lipid peroxidation

The oxidative modification of biological molecules is an essential part of the normal biological activity in the human organism. An excess in some oxidant activities does cause injury to cells and tissues. Particular attention is devoted to the oxidant activity of free radicals. An increased free radical formation in the organism is involved in the pathophysiology of several diseases. One of the events generated by free radicals interaction with biomolecules is the oxidative degradation of fatty acids. Oxidative stress is the origin or cause of lipid peroxidation and, as a consequence, of a wide variety of pathophysiological processes. Lipid peroxidation is the free-radical-induced oxidative degradation of polyunsaturated fatty acids. Biomembranes and cells are thereby disrupted, causing cell damage and cell death. As a marker of free-radical-mediated damage in the human body, the measurement of the exhaled volatile hydrocarbons, such as ethylene, is a good noninvasive method to monitor lipid peroxidation.

We have studied lipid peroxidation as a consequence of ionising radiation and heavy metals in living cells (Dumitras et al., 2004). Most heavy metals have a toxic action on human cells and may induce lipid peroxidation. Cadmium is a toxic agent which is supposed to affect the transport of ion through the cell membrane. Cadmium and calcium ionic radii are similar, so Cd can be picked up through the Ca transport mechanism. On the other hand, the Cd permeability through the calcium channel is very poor, so Cd can be considered as a blocker of the calcium channel as well. We tried to determine the extent of the toxic action of Cd *in vitro* by monitoring the ethylene concentration in the breathing air of human cells cultured in a liquid medium to which cadmium chloride was added. Cells of the human leukemic T cell line (Jurkat) were kept in a culture in RPMI 1640 medium containing 10% FBS, 1% L-glutamine and 1% penicillin streptomycin at 37°C in a humidified incubator with 5% CO_2 and 95% air.

The measurement of ethylene before and after treatment of the culture of human cells with $CdCl_2$ has shown that the concentration has increased from 0.5 ppb for control (live cells) to

1.2-1.4 ppb for dead cells, both after 5 hours and 24 hours from the treatment. The increase of ethylene content clearly demonstrates that lipid peroxidation took place owing to the toxic effect of heavy metals (Fig. 34). The measurements were performed on 10P(14) line of the CO_2 laser by means of a nitrogen flow-through system (25 sccm). The CO_2 laser, tuned off resonance on the 10P(20) line from time to time, causes a clear drop in the observed signal.

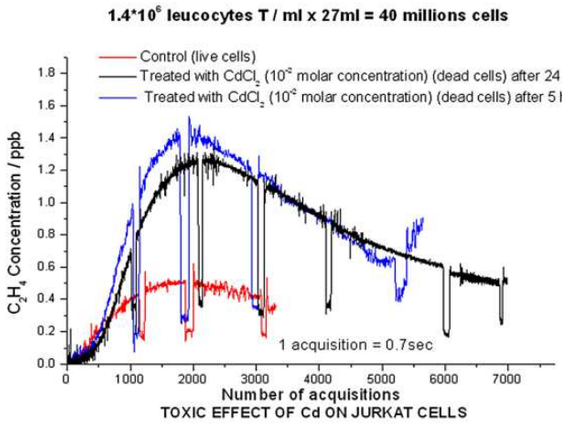

Fig. 34. Toxic effect of Cd on Jurkat cells.

The radiation damage in living matter develops along complex chains of events that follow the absorption of energy: a) physical stage: the energy transfer from the radiation to the matter leads mainly to molecular excitations and ionization; b) chemical stage: the primary reactive species (free atoms and radicals, that are usually extremely unstable), undergo secondary single reactions or a succession of reactions among each other and with their environment, causing damage to molecules of biological importance; c) biological stage: molecular changes occurring in a living organism may cause alterations in the system organization, which become macroscopically observable as biological effects. A substantial part of the total ionising radiation effect concerns water radiolysis, water being a major component of living tissues present in all biological systems. Many water ions and radicals are generated inside tissues as primary reactive species. Aqueous free radicals are very reactive and induce oxidative degradation of phospholipids in cell membranes (lipid peroxidation). The aim of our investigation was to measure the X-ray induced ethylene emission in mice breath and to analyse breath exhaled from patients under external X-ray beam therapy for cancer treatment.

For the purpose of verifying the radioinduced effect, living mice (B6C3F1 and C57B1/6J male mice, between 3 and 6 months old) have been exposed to the total body action of a 250 kV X-ray apparatus GILARDONI model CHF-320-G. At 250 kV voltage and 15 mA current by using a 0.5 mm Cu filter, the measured dose rate was 90.1 cGy/min at 68.4 cm from the source. The value of the X-ray dose given to the treated mice (9 Gy per total body) is comparable, as order of magnitude, to the therapeutic doses given to a human patient in the course of cancer treatment by radiotherapy. The mice were divided in treated and control groups. Each treated mouse received a substantial amount of X-rays in the whole body, while the control mouse received a zero dose. Samples of the breathing air have been collected before and after irradiation. The breathing air has been concentrated on active coal absorbing pellets for a time as long as 1.5 hours, successively expanded into 0.5 liters sample bags, and then transferred into the photoacoustic cell in order to perform the analysis of ethylene content. The PA analysis of ethylene content, by using the above described

procedure, takes only few minutes and, after calibration, allows for immediate data release. The radioinduced production of ethylene in the animal appears to be at clearly detectable levels, since the exhaled ethylene increases more than 4 times in the mouse breath after the irradiation (12.4 ppb for control mice before exposure, compared to 55.9 ppb for irradiated mice, after exposure) (Giubileo et al., 2003).

The cigarette smoke contains many toxic components (heavy metals, free radicals, chemicals) that may induce ethylene formation by lipid peroxidation in the lung epithelium (Dumitras et al., 2008; Giubileo et al., 2004). In order to monitor the damages caused by the inhaled smoke, we performed a breath test which gives us information about the volatile compounds under normal and stress circumstances. The exhaled air from the subject being tested was collected inside aluminized bags and then the sample gas was transferred into the measurement PA cell. In all experiments, a high value of ethylene concentration was found immediately after smoking, followed by a slower decrease. A total concentration of 4040 ppb of ethylene was measured in cigarette smoke. In the exhaled breath of a smoker, we found an ethylene concentration of 39 ppb immediately after smoking and even 1.4 ppb at half an hour from smoking a single cigarette, compared to 0.6 ppb as base (before smoking). Ethylene is dangerous for smokers because ethylene oxide is a chemical product that induces cancer in the lungs. For the moment, it is difficult to separate the exogenous and endogenous origin of the ethylene in the smoker's breath.

3.4 Measurement of human biomarkers

The application of laser photoacoustic spectroscopy for fast and precise measurements of breath biomarkers has opened up new promises for monitoring and diagnostics in recent years, especially because breath test is a non-invasive method, safe, rapid and acceptable to patients.

The detection of biomarkers in the human breath for the purpose of diagnosis has a long history. Ancient Greek physicians already knew that the aroma of human breath could provide clues to diagnosis. The perceptive clinician was alert for the sweet, fruity odor of acetone in patients with uncontrolled diabetes; the musty, fishy reek of advanced liver disease; the urine-like smell that accompanies failing kidneys; and the putrid stench of a lung abscess. Modern breath analysis is a noninvasive medical diagnostic method that distinguishes among more than 1000 compounds in exhaled breath.

Human breath includes hundreds of VOCs in low concentrations even though fewer than fifty of these are found in the majority of normal human's breath. Some of these VOCs (ethane, n-pentane, butane, ethanol, acetone) have been identified as biomarkers to some specific pathologies, including lipid peroxidation, heart failure, asthma, cystic fibrosis, diabetic ketoacidosis, alcohol intoxication, renal failure, and others. However, due to the low concentrations and presence of a large number of chemical species in exhaled air, breath analysis requires high sensitive and selective instrumentation to detect and identify the atypical concentrations of specific biomarkers (Cernat et al., 2010; Popa et al., 2011a). In order to assess the physiological meaning and the diagnostic potential of these substances, the biochemical pathways of generation have to be known.

Ethylene from the human breath is a marker of oxidant stress (in patients on hemodialisys, in acute myocardial infarction, in inflammatory diseases and ultraviolet radiation damage of human skin) and can be directly attributed to biochemical events surrounding lipid peroxidation (Dumitras et al., 2005).

Free radicals come from two major sources: endogenous and exogenous. Endogenous free radicals are produced in the body by different mechanisms whereas exogenous sources of free radicals include air pollution, ionizing radiation, cigarette smoke, inflammation etc. The ultimate step in the peroxidative chain reaction is the formation of different hydrocarbons molecules, depending on the molecular arrangement of the fatty acid involved. In the human body, the fatty acids inside the membrane lipids are mainly linoleic acid and arachidonic acid. The peroxidation of these fatty acids produces two volatile alkanes: ethylene and pentane, respectively. Both of them are considered in literature to be good biomarkers of free radical induced lipid peroxidation in humans. The fact that ethylene is highly volatile, not significantly metabolized by the body and not soluble in body fat, means that this diffuses rapidly into bloodstream after generation and it is transported to the lungs. In the lungs, the gas is excreted in the expired breath and then is collected.

Generally speaking, exhaled breath analysis (called breath test) can be represented as follows: production of the biomarker during a particular biochemical reaction or a complex metabolic process; diffusion of biomarker through tissues and input into haematic flow; possible intermediate accumulation (buffering); possible trapping of biomarker by utilization and assimilation systems or natural chemical transformation; transport to the lungs; transmembrane diffusion to the air space of lungs; diffusion of biomarker and their mixing with inhaled air in the alveolar space of lungs; release of biomarker in the breathing air; collection of a breath sample and assessment of the biomarker in the breath sample.

To get an efficient breath air sample, we used aluminized multi-patient collection bags (750 mL aluminum-coated bags-QuinTron), composed of a disposable mouthpiece and a tee-mouthpiece assembly (it includes a plastic tee and a removable one-way flutter valve). Multi-patient collection bags (Fig. 35) are designed to collect multiple samples from patients and hold a sample for maximum 6 hours.

Mouthpiece and tee-connector 0.75 L aluminum-coated bag 0.40 L discard bag

Fig. 35. Breath sample collection system.

How is properly collected a breath sample? After an approximately normal inspiration (avoiding filling the lungs at maximum), the subject places the mouthpiece in his/her mouth, forming a tight seal around it with the lips. A normal expiration is then made through the mouth, in order to empty the lungs of as much air as required to provide the alveolar sample. The first portion of the expired air goes out, after which the valve is opened the tee-piece, the remaining expired air being redirected into the collection bag. When a suitable sample is collected, the patient stops exhaling and removes the mouthpiece.

After the alveolar air sample is collected, the sample gas is transferred into the PA cell and can be analyzed immediately or later. In either case, it is recommendable to seal the large port with the collection bag port cap furnished with the collection bag. The use of the port

cap assures that the sample volume will not be lost due to a leak. Its use also avoids the contamination of the sample by gas diffusion through the one-way valve in the large port, if the sample is stored for a long period of time prior to its analysis.

Radiation therapy (also called radiotherapy, X-ray therapy, or irradiation) is the use of certain type of energy (called ionizing radiation) to kill cancer cells and shrink tumors. Radiation therapy injures or destroys cells in the area being treated by damaging their genetic material, making it impossible for these cells to continue grow and divide. Although radiation damages both cancer cells and normal cells, most normal cells can recover from the effects of radiation and function properly. The goal of radiotherapy is to damage as many cancer cells as possible, while limiting harm to nearby healthy tissue.

The effect of ionizing radiation on living cells is supposed to modify the oxidative stress status in the human body through an increase in the peroxidation processes started by the free water radicals generated by indirect radiation effect in living tissue. Important events of the peroxidation take place in the cell membranes determining the release of small linear hydrocarbon molecules through the lipid peroxidation pathways. A fraction of the hydrocarbon molecules generated in the tissue (one among them is the ethylene) will be transported to the lungs by the blood and release in the exhaled breath.

We have analyzed exhaled air from 6 patients between 32 and 77 years old receiving radiation treatment based on X-ray external beam after malign tumor surgery (Dumitras et al., 2008). Breath samples were taken from volunteers at certain time intervals (before, immediately after and at 15 minutes after the X-ray therapy). The patients received fractional doses as high as 2 to 8 Gy depending on the type of cancer. For this experiment patients were asked to exhale into sample bags at a normal exhalation flow rate.

The exhaled air sample was transferred in the PA cell and analyzed in the continuous nitrogen flux. The KOH trap inserted in the gas circuit is used to remove as much as possible the high quantity of CO_2 from the exhaled air. To subtract from the final results any influence of the interfering gases (CO_2, H_2O vapors) we applied the changing lines method, using 3 lines: 10P(14), 10P(16), and 10P(26).

We have measured the following levels of ethylene for a patient (female, 77 years old) with mammary cancer treated by X-ray therapy with a dose of 8 Gy: a) before X-ray therapy: c = 18.6 ppbV; b) Immediately after X-ray therapy: c = 23.17 ppbV; c) 15 min after the X-ray therapy: c = 10.83 ppbV. As a first observation of our measurement we see that, indeed, after the X-ray irradiation the ethylene concentration rises, showing that lipid peroxidation took place. So, it is possible to detect the process in the very first minute after irradiation. The effect of lipid peroxidation is more powerful on the cancer cells, while the healthy cells even affected have higher recovery ability. A surprising decrease in the level of ethylene concentration was observed in the exhaled air after 15 minutes, the level being even lower than the normal level of the patient (e.g. the level measured before any irradiation). This could be explained as a body reaction to the increased level of peroxidic attack: higher the rate of damage, higher the self-defense response of the human organism. Further work is required in order to verify this hypothesis.

In separate studies (Popa et al., 2011b; Popa et al., 2011c), we investigated the breath ethylene and the breath ammonia levels in patients with renal failure receiving haemodialysis (HD) treatment. Human bodies use ammonia in a number of ways, including

for the maintenance of the normal pH balance necessary to sustain life. Ammonia is processed in the liver, kidneys and skeletal muscles. Typically, ammonia and ammonium ions (in a healthy individual) are converted into urea in the liver through the urea cycle (Krebs-Henseileit cycle). The urea is then transported through the blood-stream to be excreted into urine by the kidneys. The reversibility of the process requires an equilibrium concentration of ammonia related to the blood urea nitrogen (BUN) loading of the blood. As small molecules, ammonia and ammonium ions can penetrate the blood-lung barrier, and appear in exhaled breath. In the case of kidney dysfunction, urea is unable to be excreted, causing an excessive build up of ammonia in the blood. People with kidney failure have a marked odor of ammonia ("fishy") on their breath, which can be an indicator of this disease.

Volunteer participants (Table 6) were recruited from patients receiving HD treatment at the renal dialysis clinics at the IHS Fundeni (International Healthcare Systems), Bucharest. Subjects were dialyzed 3 times per week, with a 4 h dialysis session. They were instructed to use antiseptic mouthwash before each breath sampling, to avoid oral bacteria (over 700 species of bacteria live in our mouths and can interfere with our molecules of interest). HD was accomplished with BAXTER dialysis machines using DICEA (and XENIUM) high performance cellulose diacetate hollow fibre dialyser-gamma series (DICEA 170G) with following characteristics: surface area of 1.7 m^2, ultrafiltration rate 12.5 mL/hr/mmHg, inner diameter of 200 microns and membrane thickness of 15 microns.

Patient	**Gender**	**Age**	**HD since**	**U_{preHD} (mg/dl)**	**U_{postHD} (mg/dl)**	**C_2H_4 (ppm)**			**NH_3 (ppm)**		
						before HD	during HD	after HD	before HD	during HD	after HD
P1	Male	67	2005	147	37	0.03	0.13	0.52	4.63	3.58	2.39
P2	Male	80	2004	131	39	0.23	0.51	0.93	4.28	2.82	1.53
P3	Male	79	2008	136	22	0.17	0.31	0.91	2.89	2.06	0.67
P4	Male	22	2010	135	21	0.14	0.19	0.84	5.71	4.08	3.24
P5	Male	54	2010	174	48	0.18	0.43	0.89	4.79	3.07	1.5
P6	Male	66	2005	147	66	-	-	-	2.8	2.01	1.66

Table 6. The particular data of patients and the experimental measurements of breath ethylene and ammonia concentrations (± 10% data error).

A special mention should be made: NH_3 is a highly adsorbing compound and the results of successive measurements are often altered by the molecules previously adsorbed on the pathway and cell walls. To ensure the quality of each measurement, an intensive cycle of N_2 washing was performed between samples, in order to have a maximum increase of 10% for the background photoacoustic signal. It has to be underlined that the measured photoacoustic signal is due mainly to the absorption of ammonia and ethylene, respectively, but some traces of CO_2, H_2O, ethanol, etc., influence the measurements (overall contribution is less than 10%).

Experimental measurements in order to detect traces of ethylene and ammonia were performed for a healthy volunteer (C. A. male, 26 years old) and for 6 patients with renal failure. Particular data of patients are summarized in Table 6. The exhaled air samples were collected before, during (about 1 hour after the start of HD) and immediately after the HD procedure. Analysis of pre-dialysis urea level and post-dialysis urea level (normal limit in the range of 19 - 43 mg/dL) was made at MedCenter, Bucharest (VITROS 51). The results are also presented in Table 6.

Experimental measurements of breath ethylene and ammonia concentrations for the patients (P1-P6) with renal failure and for the healthy subject (P0) were performed and the results are presented in Fig. 36. The control P0 values are 0.006 ppm ethylene and 0.25 ppm ammonia. All measurements were made at 10P(14) CO_2 laser line (10.53 μm), where the ethylene absorption coefficient has the largest value (30.4 $cm^{-1}atm^{-1}$), and at 9R(30) CO_2 laser line (9.22 μm), where the ammonia absorption coefficient has the maximum value of 57 $cm^{-1}atm^{-1}$.

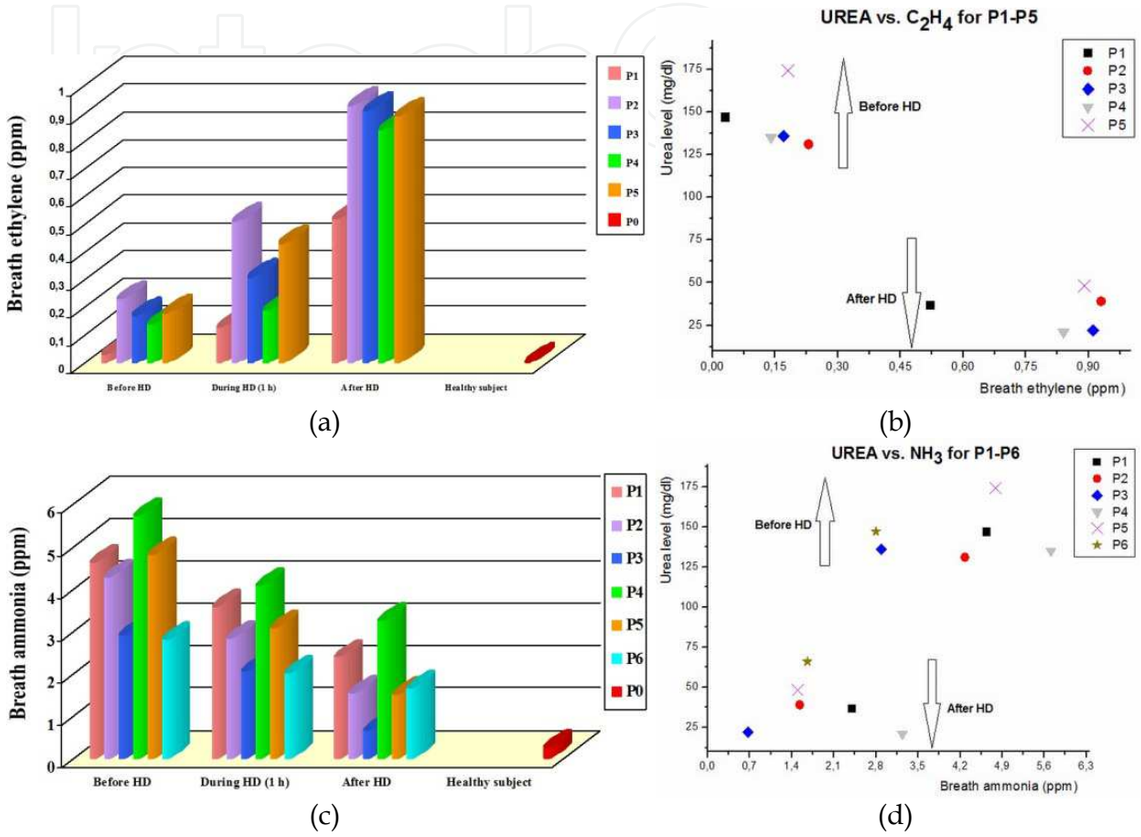

Fig. 36. Ethylene and ammonia concentrations in exhaled breath of patients under HD treatment: (a) ethylene concentrations; (b) breath ethylene concentration correlation with urea level; (c) ammonia concentrations; (d) breath ethylene concentration correlation with urea level.

As a first observation of our measurements (shown in Fig. 36a), we see that, immediately after HD treatment, the ethylene concentration increases, proving the presence of lipid peroxidation. Oxidative stress is a persistent manifestation at patients with renal failure, showing an imbalance between oxidant and antioxidant systems. HD is associated with increased oxidative stress and all treated patients are exposed to this stress. This situation appears to be due to an increased production of free radicals during HD and immediately after HD and a net reduction of many antioxidants.

In Fig. 36 (c) we can observe, as expected, a reduction of ammonia concentration in exhaled breath at patients under HD treatment, which means that ammonia detection in human breath using LPAS system can be used for determining the exact time necessary at every session for the desired state of HD for a patient with end stage renal disease and, in the same time, could serve as a broad noninvasive screen for incipient renal disease.

The most important result is the correlation found between urea data (measured by blood analysis) and the individual breath ammonia and ethylene concentrations (measured by photoacoustic technique), shown in Figs. 36 (b) and 36 (d) for six patients.

This analysis demonstrates that HD determines simultaneously a large increase of the ethylene concentration in the exhaled breath (owing to the oxidative stress) and a reduction of the ammonia concentration, correlated to the level of blood urea nitrogen.

Laser photoacoustic spectroscopy technique demonstrated that it will play an important role in the future of exhaled breath analysis. The key attributes of this technique is sensitivity, selectivity, fast and real time response and ease to use.

4. Conclusions

The applications of resonant PA spectroscopy include concentration measurements and trace gas analysis, accurate determinations of thermophysical properties, detections of dynamic processes such as gas mixing or chemical reactions, relaxation processes (determinations of collisional lifetimes of specified quantum states and routes of energy exchange in polyatomic molecules), spectroscopic experiments, studies of aerosols, etc. Trace-gas sensing is a rapidly developing field, in demand for applications such as process and air-quality measurements, atmospheric monitoring, breath diagnostics, biology and agriculture, chemistry, and security and workplace surveillance.

More than 250 different volatile organic compounds including air pollutants originating from the burning of fossil fuels, traffic, or natural sources can be identified and measured with a CO_2 laser based PA instrument. Such studies are prompted by the growing public concern about serious environmental problems such as acid rain, photochemical smog, stratospheric ozone depletion, and global climatic changes.

Breath analysis is a noninvasive medical diagnostic method that distinguishes among more than 1000 compounds in exhaled breath. Many of these compounds, if measured accurately at very low concentration levels, typically in the range of few ppbV, can be used to identify particular medical conditions. Measuring human biomarkers in exhaled breath is expected to revolutionize diagnosis and management of many diseases and may soon lead to rapid, improved, lower-cost diagnosis, which will in turn ensure expanded life spans and an improved quality of life. For example, ammonia levels in the breath can be used to determine the exact time necessary for an optimal degree of dialysis for a patient with end-stage renal disease at every session.

Trace-gas detection techniques based on PA spectroscopy make it possible to discover and control plant physiology mechanisms such as those responsible for germination, blossoming, senescence, ripening, wounding effects, post anaerobic injury, etc. Many agriculturally interesting gases (ethylene, methane, water vapor concentration, carbon dioxide, ammonia, ozone) can be measured *in situ* and in real time with CO_2 and CO laser based photoacoustic spectrometers.

In chemistry, PA spectroscopy is useful in the monitoring of chemical processes (reaction rates, equilibrium constants, enthalpies), identification of different compounds (even isomers and radicals), and dimerization of fatty acid vapors**.**

The techniques of PA spectroscopy can be extended to the detection of a wide variety of industrial gases, including benzene, hydrogen cyanide, acetylene, carbon monoxide, and carbon

dioxide, as well as a broad range of chemical warfare agents, including nerve gases (Sarin, Soman, Tabun), blistering agents (phosgene, mustard gas), and poisonous gases (hydrogen cyanide), explosives (TNT, PETN), and harmful drugs (heroin, morphine, narcotine).

Our previous research on LPAS (Dumitras et al., 1993; Dutu et al., 1994a; Dutu et al., 1994b; Dumitras et al., 1996a; Dumitras et al., 1996b; Cristescu et al., 1997; Cristescu et al., 2000a) has led to the development of new applications in plant physiology (seed germination, ripening of climacteric fruits, plant response to pathogen infection) (Cristescu et al., 1998; Cristescu et al., 1999; Lai et al., 2003), measurement of gas absorption coefficients (ethylene, ammonia) (Cristescu et al., 2000b; Dumitras et al., 2007; Dumitras et al., 2011), and medicine (cultures of human cells doped with heavy metals, ionizing radiation damage in living organisms, lipid peroxidation in lung epithelium following the inhalation of cigarette smoke, exhaled breath from patients treated by anti-tumor radioisotope therapy and patients under HD treatment) (Giubileo et al., 2003; Dumitras et al., 2004; Giubileo et al., 2004; Dumitras et al., 2005; Cernat et al., 2010; Popa et al., 2011a; Popa et al., 2011b; Popa et al., 2011c; Popa & Matei, 2011).

Extensions of various aspects of this work are currently being pursued in our laboratory.

5. References

Angeli, G.Z.; Solyom, A.M.; Miklos, A. & Bicanic, D.D. (1992). Calibration of a Windowless Photoacoustic Cell for Detection of Trace Gases. *Anal. Chem.,* Vol.64, No.2, (January 1992), pp. 155-158, ISSN 0003-2700

Beck, S.M. (1985). Cell Coatings to Minimize Sample (NH_3 and N_2H_4) Adsorption for Low-Level Photoacoustic Detection. *Appl. Opt.,* Vol.24, No.12, (June 1985), pp. 1761-1763, ISSN 0003-6935

Bernegger, S. & Sigrist, M.W. (1987). Longitudinal Resonant Spectrophone for CO-laser Photoacoustic Spectroscopy. *Appl. Phys. B,* Vol.44, No.2, (October 1987), pp. 125-132, ISSN 0946-2171

Bijnen, F.G.; Reuss, J. & Harren, F.J.M. (1996). Geometrical Optimization of a Longitudinal Resonant Photoacoustic Cell for Sensitive and Fast Trace Gas Detection. *Rev. Sci. Instrum.,* Vol.67, No.8, (August 1996), pp. 2914-2923, ISSN 0034-6748

Bratu, A.M.; Popa, C. ; Matei, C. ; Banita, S.; Dutu, D.C.A. & Dumitras, D.C. (2011). Removal of Interfering Gases in Breath Biomarker Measurements. *J. Optoelectron. Adv. Mater.,* Vol.13, No. 8, (August 2011), pp. 1045-1050, ISSN 1454-4164

Brewer, J. & Bruce, C.W. (1978). Photoacoustic Spectroscopy of NH_3 at the 9-μm and 10-μm $^{12}C^{16}O_2$ Laser Wavelengths. *Appl. Opt.,* Vol.17, No.23, (December 1978), pp. 3746-3749, ISSN 0003-6935

Brewer, R.J.; Bruce, C.W. & Mater, J.L. (1982). Optoacoustic Spectroscopy of C_2H_4 at the 9- and 10-μm $C^{12}O_2{}^{16}$ Laser Wavelengths. *Appl. Opt.,* Vol.21, No.22, (November 1982), pp. 4092-4100, ISSN 0003-6935

Cernat, R.; Matei, C.; Bratu, A.M.; Popa, C.; Dutu, D.C.A.; Patachia, M.; Petrus, M.; Banita, S. & Dumitras, D.C. (2010). Laser Photoacoustic Spectroscopy Method for Measurements of Trace Gas Concentrations from Human Breath. *Rom. Rep. Phys.,* Vol.62, No.3, pp. 610-616, ISSN 1221-1451

Crane, R.A. (1978). Laser Optoacoustic Absorption Spectra for Various Explosive Vapors. *Appl. Opt.,* Vol.17, No.13, (July 1978), pp. 2097-2102, ISSN 0003-6935

Cristescu, S.; Dumitras D.C. & Godeanu, A. (1999). Role of Ethylene in the Germination Metabolism of Ricinus Communis. *Proc. Tenth International Conference "Photoacoustic*

and Photothermal Phenomena", Vol.463, F. Scudieri, M. Bertolotti (Eds), pp. 652-654, American Institute of Physics, ISBN 978-1-563-96805-3, Melville, NY, USA

Cristescu, S.; Dumitras, D.C. & Duțu, D.C.A. (1998). Photoacoustic Detection of Ethylene Released by Biological Samples under Stress Conditions. *Proc. SPIE ROMOPTO '97: Fifth Conference on Optics,* Vol.3405, V.I. Vlad, D.C. Dumitras (Eds.), pp. 627-631, SPIE, ISBN 978-0-819-42857-8, Bellingham, WA, USA

Cristescu, S.; Dumitras, D.C. & Dutu, D.C.A. (2000a). Characterization of a Resonant Cell Using the Acoustic Transmission Line Model. *Proc. SPIE SIOEL '99: Sixth Symposium on Optoelectronics,* Vol.4068, T. Necsoiu, M. Robu, D.C. Dumitras (Eds.), pp. 263-272, SPIE, ISBN 978-0-819-43705-1, Bellingham, WA, USA

Cristescu, S.; Dumitras, D.C. & Dutu, D.C.A. (2000b). Ammonia and Ethene Absorption Measurements with a Tunable CO_2 Laser-Based Photoacoustic Trace Gas Detector. *Proc. SPIE ALT '99 International Conference on Advanced Laser Technologies,* Vol.4070, V.I. Pustovoy, V.I. Konov (Eds.), pp. 457-464, SPIE, ISBN 978-0-819-43707-5, Bellingham, WA, USA

Cristescu, S.; Dumitras, D.C.; Dutu, D.C.A. & Mujat, C. (1997). Real-Time Detection System for Laser Photoacoustic Applications. *Rom. Rep. Phys.,* Vol.49, No.8-9-10, pp. 757-768, ISSN 1221-1451

Davidson, J.; Gutow, J.H. & Zare, R.N. (1990). Experimental Improvements in Recording Gas-Phase Photoacoustic Spectra. *J. Phys. Chem.,* Vol.94, No.10, (May 1990), pp. 4069-4073, ISSN 0022-3654

Dewey, C.F. (1977). Design of Optoacoustic Systems. In *Optoacoustic Spectroscopy and Detection*, Ch. 3, Y.-H. Pao (Ed.), 47-77, Academic, ISBN 978-0-125-44159-9, New York, NY, USA

Dumitras, D. C.; Alexandrescu, R. & Morjan, I. (1993). Laser Absorption Measurements Using Photoacoustic Detection. In *Proc. 10-th Int. FASE Symposium*, D. Rucinski (Ed.), 189-192, ICPE Publishing House, Bucharest, Romania

Dumitras, D.C.; Banita, S.; Bratu, A.M.; Cernat, R.; Dutu, D.C.A.; Matei, C.; Patachia, M.; Petrus, M. & Popa, C. (2010). Ultrasensitive CO_2 Laser Photoacoustic System. *Infrared Phys. Technol.,* Vol.53, No.5, (September 2010), pp. 308-314, ISSN 1350-4495

Dumitras, D.C.; Dutu, D.C.; Comaniciu, N. & Draganescu, V. (1976). Sealed-Off CO_2 Lasers. *Rev. Roum. Phys.,* Vol.21, No.6, pp. 559-568, ISSN 0035-4090

Dumitras, D.C.; Dutu, D.C.; Comaniciu, N.; Draganescu, V.; Alexandrescu, R. & Morjan, I. (1981). Frequency Stabilized CO_2 Laser Design. *Rev. Roum. Phys.,* Vol.26, No.5, pp. 485-498, ISSN 1221-1451

Dumitras, D.C.; Dutu, D.C.; Draganescu, V. & Comaniciu, N. (1985). *Frequency Stabilization of CO_2 Lasers*. Preprint LOP-55, CIP Press, Bucharest, Romania

Dumitras, D.C.; Dutu, D.C.; Matei, C.; Magureanu, A.M.; Petrus, M. & Popa, C. (2007). Laser Photoacoustic Spectroscopy: Principles, Instrumentation, and Characterization. *J. Optoelectr. Adv. Mater.,* Vol.9, No.12, (December 2007), pp. 3655-3701, ISSN 1454-4164

Dumitras, D.C.; Dutu, D.C.; Matei, C.; Magureanu, A.M.; Petrus, M.; Popa C. & Patachia, M. (2008). Measurements of Ethylene Concentration by Laser Photoacoustic Techniques with Applications at Breath Analysis. *Rom. Rep. Phys.,* Vol.60, No.3, pp. 593-602, ISSN 1221-1451

Dumitras, D.C.; Dutu, D.C.A.; Cristescu, S. & Mujat, C. (1996a). Laser Photoacoustic Spectroscopy: A Powerful Tool for Trace Gas Measurements. *Proc. SPIE 17th Congress of the International Commission for Optics: Optics for Science and New Technology,* Vol.2778, J.–S. Chang, J.-H. Lee, C.-H. Nam (Eds.), pp. 670-671, SPIE, ISBN 978-0-819-42164-7, Bellingham, WA, USA

Dumitras, D.C.; Dutu, D.C.A.; Cristescu, S. & Mujat, C. (1996b). Trace Gas Analysis Using Laser Photoacoustic Spectroscopy Methods. *Optoelectronica,* Vol.4, pp. 21-27

Dumitras, D.C.; Dutu, D.C.A.; Matei, C.; Cernat, R.; Banita, S.; Patachia, M.; Bratu, A.M.; Petrus, M. & Popa, C. (2011). Evaluation of Ammonia Absorption Coefficients by Photoacoustic Spectroscopy for Detection of Ammonia Levels in Human Breath. *Laser Phys.,* Vol.21, No.4, (April 2011), pp. 796-800, ISSN 1555-6611

Dumitras, D.C.; Giubileo, G. & Puiu, A. (2005). Investigation of Human Biomarkers in Exhaled Breath by Laser Photoacoustic Spectroscopy. *Proc. SPIE Advanced Laser Technologies 2004,* Vol.5850, I.A. Shcherbakov, A. Giardini, V.I. Konov, V.I. Pustovoy (Eds.), pp. 111-121, SPIE, ISBN 978-0-819-45847-6, Bellingham, WA, USA

Dumitras, D.C.; Puiu, A.; Cernat, R.; Giubileo, G. & Lai, A. (2004). Laser Photoacoustic Spectroscopy: A Powerful Tool for Measurement of Trace Gases of Biological Interest at Sub-ppb Level. *Molec. Cryst. Liquid Cryst. J.,* Vol.418, No.1, (January 2004), pp. 217/[945]-227/[955], ISSN 1542-1406

Dumitras, D.C.; Sporea, D. & Dutu, D.C.A. (2006). Set-Up for Power Calibration Transfer at CO_2 Laser Wavelength. *Proc. SPIE Advanced Laser Technologies 2005,* Vol.6344, I.A. Shcherbakov, K. Xu, Q. Wang, A.V. Priezzhev, V.I. Pustovoy (Eds.), pp. 643-653, SPIE, ISBN 978-0-819-46420-0, Bellingham, WA, USA

Dutu, D.C.; Draganescu, V.; Comaniciu, N. & Dumitras, D.C. (1985). Plasma Impedance and Optovoltaic Effect in Sealed-Off CO_2 Lasers. *Rev. Roum. Phys.,* Vol.30, No.2, pp. 127-130, ISSN 0035-4090

Dutu, D.C.A.; Cristescu, S. & Dumitras, D.C. (1994b). Measurement of Photoacoustic Signal and Noises in a Sensitive Spectrophone with a Frequency Stabilized CO_2 Laser. In *Proc. SPIE ROMOPTO'94-Fourth Conference in Optics,* Vol.2461, V.I. Vlad (Ed.), pp. 308-316, SPIE, ISBN 978-0-819-41813-5, Bellingham, WA, USA

Dutu, D.C.A.; Dumitras, D.C.; Cristescu, S. & Sarkozy, L. (1994a). Evaluation of Photoacoustic Signal and Noises in a Sensitive Spectrophone Irradiated by a CO_2 Laser Beam. *Rom. Rep. Phys.,* Vol.46, No.7-8, pp. 639-644, ISSN 1221-1451

Fink, T.; Büscher, S.; Gäbler, R.; Yu, Q.; Dax, A. & Urban, W. (1996). An Improved CO_2 Laser Intracavity Photoacoustic Spectrometer for Trace Gas Analysis. *Rev. Sci. Instrum.,* Vol.67, No.11, (November 1996), pp. 4000-4004, ISSN 0034-6748

Fung, K. H. & Lin, H.-B. (1986). Trace Gas Detection by Laser Intracavity Photothermal Spectroscopy. *Appl. Opt.,* Vol.25, No.5, (March 1986), pp. 749-752, ISSN 0003-6935

Gandurin, A. L.; Gerasimov, S.B.; Zheltukhin, A.A.; Konovalov, I.P.; Kornilov, S.T.; Mel'nik, G.F.; Mikhalevich, Yu.Yu.; Ogurok, D.D.; Petrishchev, V.A. & Chirikov, S.N. (1986). Optoacoustic Gas Analyzer for NO, NO_2, NH_3, C_2H_4, and Saturated Hydrocarbon Pollutants. *Zh. Prikl. Spektrosk.,* Vol.45, No.2, (August 1986), pp. 337-343, ISSN 0514-7506

Gerlach, R. & Amer, N.M. (1980). Brewster Window and Windowless Resonant Spectrophones for Intracavity Operation. *Appl. Phys.A,* Vol.23, No.3, (November 1980), pp. 319-326, ISSN 0947-8396

Giubileo, G.; DeDominicis, L.; Lombardi, C.C.; Mancini, C.; Antonini, A. & Dumitras, D.C. (2003). Detectability by Photoacoustic Spectroscopy of X-Ray Induced Ethylene in Mice Breath. *Proc. SPIE ALT'02 International Conference on Advanced Laser Technologies ,* Vol.5147, H.P. Weber, V.I. Konov, T. Graf (Eds.), pp. 219-225, SPIE, ISBN 978-0-819-45017-3, Bellingham, WA, USA

Giubileo, G.; Puiu, A. & Dumitras, D.C. (2004). Detection of Ethylene in Smokers Breath by Laser Photoacoustic Spectroscopy. *Proc. SPIE ALT'03 International Conference on Advanced*

Laser Technologies: Biomedical Optics, Vol.5486, R.K. Wang, J.C. Hebden, A.V. Priezzhev, V.V. Tuchin (Eds.), pp. 280-286, SPIE, ISBN 978-0-819-45418-8, Bellingham, WA, USA

Harren, F.J.M. & Reuss, J. (1997). Spectroscopy, Photoacoustic, In *Encyclopedia of Applied Physics*, Vol.19, G.L. Trigg (Ed.), 413-435, VCH Publishers, ISBN 978-3-527-40478-0, New York, USA

Harren, F.J.M.; Bijnen, F.G.C.; Reuss, J.; Voesenek, L.A.C.J. & Blom, C.W.P.M. (1990a). Sensitive Intracavity Photoacoustic Measurements with a CO_2 Waveguide Laser. *Appl. Phys. B,* Vol.50, No. 2, (February 1990), pp. 137-144, ISSN 0946-2171

Harren, F.J.M.; Reuss, J.; Woltering, E.J. & Bicanic, D.D. (1990b). Photoacoustic Measurement of Agriculturally Interesting Gases and Detection of C_2H_4 Below the ppb Level. *Appl. Spectrosc.,* Vol.44, No.8, (September 1990), pp. 1360-1368, ISSN 0003-7028

Henningsen, J. & Melander, N. (1997). Sensitive Measurement of Adsorption Dynamics with Nonresonant Gas Phase Photoacoustics. *Appl. Opt.,* Vol.36, No. 27, (September 1997), pp. 7037-7045, ISSN 0003-6935

Hubert, M.H. (1983). *Laser Optoacustic Detector Measurement of Signatures of a Selection of Environmental Contaminants.* Rep. No. 83-715-1, Ultra Lasertech Inc., Mississauga, Canada

Karbach, A. & Hess, P. (1985). High Precision Acoustic Spectroscopy by Laser Excitation of Resonant Modes. *J. Chem. Phys.,* Vol.83, No.3, (August 1985), pp. 1075-1084, ISSN 0021-9606

Kavaya, M.J.; Margolis, J.S. & Shumate, M.S. (1979). Optoacoustic Detection Using Stark Modulation. *Appl. Opt.,* Vol.18, No.15, (August 1979), pp. 2602-2606, ISSN 0003-6935

Koch, K.P. & Lahmann, W. (1978). Optoacoustic Detection of Sulphur Dioxide Below the Parts per Billion Level. *Appl. Phys. Lett.,* Vol.32, No.5, (March 1978), pp. 289-291, ISSN 0003-6951

Kosterev, A.A.; Bakhirkin, Y.A. & Tittel, F.K. (2005). Ultrasensitive Gas Detection by Quartz-Enhanced Photoacoustic Spectroscopy in the Fundamental Molecular Absorption Bands Region. *Appl. Phys. B,* Vol.80, No.1, (January 2005), pp. 133-138, ISSN 0946-2171

Kritchman, E.; Shtrikman, S. & Slatkine, M. (1978). Resonant Optoacoustic Cells for Trace Gas Analysis. *J. Opt. Soc. Am.,* Vol.68, No.9, (September 1978), pp. 1257-1271, ISSN 1084-7529

Lai, A.; DeDominicis, L.; Francucci, M.; Giorgi, M.; Giubileo, G. & Dumitras, D.C. (2003). Detection of Ethylene Traces by Photoacoustic Spectroscopy. *Proc. SPIE Third GR-I International Conference on New Laser Technologies and Applications,* Vol.5131, A. Carabelas, G. Baldacchini, P. Di Lazzaro, D. Zevgolis (Eds.), pp. 295-299, SPIE, ISBN 978-0-819-44997-9, Bellingham, WA, USA

Meyer, P.L. & Sigrist, M.W. (1990). Atmospheric Pollution Monitoring Using CO_2-Laser Photoacoustic Spectroscopy and Other Techniques. *Rev. Sci. Instrum.,* Vol.61, No.7, (July 1990), pp. 1779-1807, ISSN 0034-6748

Miklós, A. & Lörincz, A. (1989). Windowless Resonant Acoustic Chamber for Laser-Photoacoustic Applications. *Appl. Phys. B,* Vol.48, No.3, (April 1989), pp. 213-218, ISSN 0721-7269

Nägele, M. & Sigrist, M.W. (2000). Mobile Laser Spectrometer with Novel Resonant Multipass Photoacoustic Cell for Trace-Gas Sensing. *Appl. Phys. B,* Vol.70, No.6, (June 2000), pp. 895-901, ISSN 0946-2171

Nodov, E. (1978). Optimization of Resonant Cell Design for Optoacoustic Gas Spectroscopy (H-Type). *Appl. Opt.,* Vol.17, No.7, (April 1978), pp. 1110-1119, ISSN 0003-6935

Olaffson, A.; Hammerich, M.; Bülow, J. & Henningsen, J. (1989). Photoacoustic Detection of NH_3 in Power Plant Emission with a CO_2 Laser. *Appl. Phys. B,* Vol.49, No.2, (August 1989), pp. 91-97, ISSN 0946-2171

Olafsson, A.; Hammerich, M. & Henningsen, J. (1992). Photoacoustic Spectroscopy of C_2H_4 with a Tunable CO_2 Laser. *Appl. Opt.,* Vol.31, No.15, (May 1992), pp. 2657-2668, ISSN 0003-6935

Persson, U.; Marthinsson, B.; Johansson, J. & Eng, S.T. (1980). Temperature and Pressure Dependence of NH_3 and C_2H_4 Absorption Cross Sections at CO_2 Laser Wavelengths. *Appl. Opt.,* Vol.19, No.10, (May 1980), pp.1711-1715, ISSN 0003-6935

Popa, C. & Matei, C. (2011). Photoacoustic Assessment of Oxidative Stress in Dialysis and Radiotherapy by LPAS System. *Optoelectron. Adv. Mater. – Rapid Commun.*, Vol. 5, No.11, (November 2011), pp. 1237-1242, ISSN 1842-6573

Popa, C., Bratu, A.M.; Cernat, R.; Dutu, D.C.A. & Dumitras, D.C. (2011a). Spectroscopic Studies of Ethylene and Ammonia as Biomarkers at Patients with Different Medical Disorders. *U. P. B. Sci. Bull., Series A,* Vol.73, No.2, pp. 167-174, ISSN 1223-7027

Popa, C.; Bratu, A.M.; Matei, C.; Cernat, R.; Popescu, A. & Dumitras, D.C. (2011b). Qualitative and Quantitative Determination of Human Biomarkers by Laser Photoacoustic Spectroscopy Methods. *Laser Phys.,* Vol.21, No.7, (July 2011), pp. 1336-1342, ISSN 1555-6611

Popa, C.; Cernat, R.; Dutu, D.C.A. & Dumitras, D.C. (2011c). Ethylene and Ammonia Traces Measurements from the Patients Breath with Renal Failure via LPAS Method. *Appl. Phys. B,* Vol.105, No.3, (November 2011), pp. 669-674, ISSN 0946-2171

Pushkarsky, M.B.; Weber, M.E.; Baghdassarian, O.; Narasimhan, L.R. & Patel, C.K.N. (2002). Laser-Based Photoacoustic Ammonia Sensors for Industrial Applications. *Appl. Phys. B,* Vol.75, No.4-5, (April 2002), pp. 391-396, ISSN 0946-2171

Rooth, R.A.; Verhage, A.J.L. & Wouters, L.W. (1990). Photoacoustic Measurement of Ammonia in the Atmosphere: Influence of Water Vapor and Carbon Dioxide. *Appl. Opt.,* Vol.29, No. 25, (September 1990), pp. 3643-3653, ISSN 0003-6935

Rosengren, L.-G. (1975). Optimal Optoacoustic Detector Design. *Appl. Opt.,* Vol.14, No.8, (August 1975), pp. 1960-1976, ISSN 0003-6935

Ryan, J.S.; Hubert, M.H. & Crane, R.A. (1983). Water Vapor Absorption at Isotopic CO_2 Laser Wavelengths. *Appl. Opt.,* Vol.22, No.5, (March 1975), pp. 711-717, ISSN 0003-6935

Sauren, H.; Bicanic, D.; Jelink, H. & Reuss, J. (1989). High-Sensitivity, Interference-Free, Stark-Tuned CO_2 Laser Photoacoustic Sensing of Urban Ammonia. *J. Appl. Phys.,* Vol.66, No.10, (November 1989), pp. 5085-5087, ISSN 0021-4922

Siegman, A.E. (1986). *Lasers*, University Science Books, ISBN 978-0-935-70211-3, Sausalito, CA, USA

Sigrist, M.W.; Bernegger, S. & Meyer, P.L. (1989). Atmospheric and Exhaust Air Monitoring by Laser Photoacoustic Spectroscopy, In *Topics in Current Physics "Photoacoustic, Photothermal and Photochemical Processes in Gases"*, Ch.7, Vol.46, P. Hess (Ed.), 173-211, Springer, ISBN 978-3-540-51392-2, Berlin, Germany

Thomas III, L.J.; Kelly, M.J. & Amer, N.M. (1978). The Role of Buffer Gases in Optoacoustic Spectroscopy. *Appl. Phys. Lett.,* Vol.32, No.11, (June 1978), pp. 736-738, ISSN 0003-6951

Thöny, A. & Sigrist, M.W. (1995). New Developments in CO_2-Laser Photoacoustic Monitoring of Trace Gases. *Infrared Phys. Technol.,* Vol.36, No.2, (February 1995), pp. 585-615, ISSN 1350-4495

Tonelli, M.; Minguzzi, P. & Di Lieto, A. (1983). Intermodulated Optoacoustic Spectroscopy. *J. Physique (Colloque C6),* Vol.44, No.10, (October 1983), pp. 553-557, ISSN 0449-1947

Zharov, V.P. & Letokhov, V.S. (1986). *Laser Optoacoustic Spectroscopy*, Vol.37, Springer, ISBN 978-3-540-11795-4, Berlin, Germany

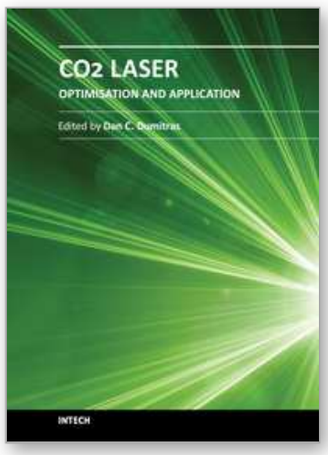

CO2 Laser - Optimisation and Application

Edited by Dr. Dan C. Dumitras

ISBN 978-953-51-0351-6
Hard cover, 436 pages
Publisher InTech
Published online 21, March, 2012
Published in print edition March, 2012

The present book includes several contributions aiming a deeper understanding of the basic processes in the operation of CO2 lasers (lasing on non-traditional bands, frequency stabilization, photoacoustic spectroscopy) and achievement of new systems (CO2 lasers generating ultrashort pulses or high average power, lasers based on diffusion cooled V-fold geometry, transmission of IR radiation through hollow core microstructured fibers). The second part of the book is dedicated to applications in material processing (heat treatment, welding, synthesis of new materials, micro fluidics) and in medicine (clinical applications, dentistry, non-ablative therapy, acceleration of protons for cancer treatment).

INTECH
open science | open minds

InTech Europe
University Campus STeP Ri
Slavka Krautzeka 83/A
51000 Rijeka, Croatia
Phone: +385 (51) 770 447
Fax: +385 (51) 686 166
www.intechopen.com

InTech China
Unit 405, Office Block, Hotel Equatorial Shanghai
No.65, Yan An Road (West), Shanghai, 200040, China
中国上海市延安西路65号上海国际贵都大饭店办公楼405单元
Phone: +86-21-62489820
Fax: +86-21-62489821

IntechOpen